Investigating the Costs and Benefits of Controllable Inlet Orifice Hydraulic Diameter in Microchannel Cooling Devices

by

Brent A. Odom

A Dissertation Presented in Partial Fulfillment
of the Requirements for the Degree
Doctor of Philosophy

Approved February 2012 by the
Graduate Supervisory Committee:

Patrick Phelan, Chair
Marcus Herrmann
Amaneh Tasooji
Don Holcomb
Steven Trimble

ARIZONA STATE UNIVERSITY

May 2012

ABSTRACT

Recent literature indicates potential benefits in microchannel cooling if an inlet orifice is used to suppress pressure oscillations that develop under two-phase conditions. This study investigates the costs and benefits of using an adjustable microchannel inlet orifice. The focus is on orifice effect during steady-state boiling and critical heat flux (CHF) in the channels using R134a in a pumped refrigerant loop (PRL). To change orifice size, a dam controlled with a micrometer was placed in front of 31 parallel microchannels. Each channel had a hydraulic diameter of 0.235 mm and a length of 1.33 cm.

For steady state two-phase conditions, mass fluxes of 300 kg m^{-2} s^{-1} and 600 kg m^{-2} s^{-1}were investigated. For orifice sizes with a hydraulic diameter to unrestricted hydraulic diameter (D_h:$D_{h,ur}$) ratio less than 35 percent, oscillations were reduced and wall temperatures fell up to 1.5 °C.

Critical heat flux data were obtained for 7 orifice sizes with mass fluxes from 186 kg m^{-2} s^{-1} to 847 kg m^{-2} s^{-1}. For all mass fluxes and inlet conditions tested, CHF values for a D_h:$D_{h,ur}$ ratio of 1.8 percent became increasingly lower (up to 37 W cm^{-2} less) than those obtained with larger orifices. An optimum orifice size with D_h:$D_{h,ur}$ of 35 percent emerged, offering up to 5 W cm^{-2} increase in CHF over unrestricted conditions at the highest mass flux tested, 847 kg m^{-2} s^{-1}.

These improvements in cooling ability with inlet orifices in place under both steady-state and impending CHF conditions are modest, leading to the conclusion that inlet orifices are only mildly effective at improving heat transfer coefficients.

Stability of the PRL used for experimentation was also studied and improved. A vapor compression cycle's (VCC) proportional, integral, and derivative controller was found to adversely affect stability within the PRL and cause premature CHF. Replacing the VCC with an ice water heat sink maintained steady pumped loop system pressures and mass flow rates. The ice water heat sink was shown to have energy cost savings over the use of a directly coupled VCC for removing heat from the PRL.

ACKNOWLEDGEMENTS

First I would like to thank my advisor, Patrick Phelan, for his advice and guidance over the past five years. I have thoroughly enjoyed learning from Jon Sherbeck for the last three years and would not have reached this point without his help. Mark Miner and Carlos Ortiz have graciously and selflessly given me their time, help, and thoughts since we began working together. I am also in debt to Todd Otanicar for introducing me to my research topic and to Rob Taylor for his help at various points along the way.

This work is supported by the Office of Naval Research as a MURI award (prime award number N00014-07-1-0723).

TABLE OF CONTENTS

Page

CHAPTER Page

CHAPTER Page

LIST OF TABLES

LIST OF FIGURES

Figure Page

Figure Page

Figure Page

NOMENCLATURE

A = area (m^2)

c = Specific Heat (J kg^{-1} °C^{-1})

CHF = critical heat flux (W cm^{-2})

D = Diameter (m)

f = Frequency (Hz)

$G(f)$ = Gain (dimensionless)

G = mass flux (kg m^{-2} s^{-1})

h = Convective heat transfer coefficient (W m^{-2} °C^{-1})

h = enthalpy (kJ kg^{-1})

k = thermal conductivity (W cm^{-1} K^{-1})

L = length (cm)

m = slope

$\dot{m}$ = mass flow rate (g s^{-1})

P = Pressure (kPa)

PID = Proportional, Integral, and Derivative

PRL = Pumped Refrigerant Loop

q'' = heat flux

Q = input power (W)

T = Temperature (°C)

U = uncertainty

v = velocity (m s^{-1})

V = Volume (m^3)

VCC = Vapor Compression Cycle

Greek Symbols

ρ = density (kg m^{-3})

τ = time constant (sec)

Δ = difference

μ = micro

σ = standard deviation

Subscripts

a = average

avg = average

act = Actual

c = condensing; cross sectional

e = estimated; exit

ei = evaporator inlet

h = hydraulic

i = inlet

l = lower

m = maximum

o = outlet

r = refrigerant

s = surface

ur = unrestricted

w = wall

wo = (evaporator) wall outlet

Chapter 1: Introduction

1.1 Problem Statement and Background

For high powered electronics, the ability to remove high-heat-flux while maintaining low device temperatures is progressively more important. The Office of Naval Research (ONR) has established 1000 W cm^{-2} as a goal for its researchers regarding heat removal from electronic chips or surfaces. Microchannel cooling is one method of potentially reaching this goal; however, for liquid flow, the sensible heat gain can result in large temperature rise between inlet and outlet of the microchannels. This is passed to the cooled electronic device, potentiating problems with thermal expansion coefficient mismatch in device materials. Two-phase flow offers the large heat capacity of latent heat with minimal temperature change across the microchannels (Ulrich & Brown, 2006). One impediment to taking advantage of two-phase conditions in microchannel cooling is early onset of critical heat flux (CHF) during sub-cooled or saturated boiling caused by flow instabilities.

The flow instabilities of greatest concern in microchannel flow are pressure oscillations and parallel channel instability (Bergles & Kandlikar, 2005). Pressure oscillations establish themselves when there is a compressible volume present upstream of the microchannels and pressure drop becomes high enough that the pump driving flow begins to struggle (Boure, Bergles, & Tong, 1972). Parallel channel instability occurs when a bubble develops in a single channel, it propagates upstream into the inlet plenum, and is then redistributed into neighboring channels. These types of flow reversals and interruptions tend to

decrease heat transfer coefficients and increase microchannel wall temperatures (Qu & Mudawar, 2003).

Flow instabilities can cause pre-mature CHF and device burnout. Pre-mature CHF occurs when an instability interrupts flow rate in one or more of the microchannels and allows vapor to form more rapidly at the cooled surface than would have occurred otherwise. Experiments investigating various aspects of flow in microchannels showed that a control valve upstream of the inlet plenum of the test section eliminated the pressure drop oscillations due to upstream compressible volumes; however, they did not eliminate parallel channel instability (Qu & Mudawar, 2003). Bergles and Kandlikar (2005) theorized that if Qu and Mudawar had installed inlet orifices in front of each individual channel, both instabilities could have been eliminated. Since then, it has been shown by a number of researchers that instabilities can be delayed or eliminated with an orifice in front of each individual microchannel (Kosar, Kuo, & Peles, 2006; Kuan & Kandlikar, 2006; Park, Thome, & Michel, 2009).

Those studies used orifices with fixed hydraulic diameter (D_h). The current study used a microchannel test section design with an adjustable inlet orifice D_h. This allowed experimental results and conclusions to cover a broad range of mass flux, heat flux, and orifice sizes. Orifice size could be changed mid-experiment to enhance understanding of inlet orifice effect. The test section design was capable of withstanding repeated cycling to the high temperatures associated with CHF.

1.2 Dissertation Organization

This dissertation studies the costs and benefits of an adjustable inlet orifice used in microchannel cooling with R134a as the working fluid in a pumped refrigerant loop (PRL). Chapter 1 begins with an introduction to stability problems in microchannel flow, and explains the need for a more detailed understanding of inlet orifice effect on microchannel cooling device performance. Chapter 2 describes the effects of various inlet orifice hydraulic diameters (D_h) on pressure oscillations and wall temperatures under steady state conditions. Findings relating to PRL stability are discussed in Chapter 3. Chapter 4 describes orifice effect on CHF values, wall temperatures, and heat transfer coefficients attained at different mass fluxes. Chapter 5 summarizes the conclusions from each chapter, covers implications of the study as a whole, and outlines suggestions for future work. Each chapter retains its original abstract and conclusions. References are in a cumulative reference section at the end of the dissertation.

Chapter 2: Microchannel Two-Phase Flow Oscillation Control with an Adjustable Inlet Orifice

Abstract

This work describes the experimental setup, method, and results of utilizing a micrometer to move an adjustable orifice immediately in front of an array of microchannels. Research by others indicates potential for significant improvement in delaying critical heat flux and increasing heat transfer coefficients when placing an orifice in front of each individual channel of a microchannel array. The experimental setup in this work allows incremental orifice size changes. This ability allows the experimentalist to find which orifice size provides enough pressure drop immediately in front of the channels to reduce oscillations. The design also allows for rapid change of orifice size without having to remove and replace any components of the test setup. Signal analysis methods were used to identify frequency and amplitude of pressure and temperature oscillations. Low mass flux experiments (300 kg m^{-2} s^{-1} and 600 kg m^{-2} s^{-1} of R134a in a pumped loop) showed reduced channel wall temperatures with smaller orifice sizes. The orifice concept was found to be more effective at reducing oscillations for the higher 600 kg m^{-2} s^{-1} flow rate.

2.1 Introduction

2.1.1 Motivation

The removal of high heat flux from electronics devices continues to be a problem, especially for defense applications. The Office of Naval Research goal is to maintain chip temperatures below 60 °C while removing 1000 W cm^{-2}. In

electronic applications, it is desirable to maintain a low chip temperature in order to increase processing speeds and avoid chip burnout. One efficient method of heat removal is to use two-phase cooling in mini or microchannels. Two-phase cooling tends to keep the chip surface temperature more even from inlet to outlet of microchannels than single phase (Bergles & Kandlikar, 2005), and tends to have a higher heat transfer coefficient. Unfortunately, for parallel microchannels, measures must be taken to prevent flow reversal and oscillations, maldistribution among channels, or other flow instabilities. Recently, researchers have shown that an inlet orifice placed in front of or built directly into the microchannel design produces a pressure drop that can effectively prevent these problems (Kuan & Kandlikar, 2006; Park et al., 2009; Koşar et al., 2006). This was mentioned as a solution for larger channels in a 1972 article by Boure, Bergles and Tong (1973). It may be advantageous to be able to control the proposed pressure drop in front of the parallel microchannels to respond to the needs of the electronic device being cooled. Changing a pump speed will not be the most responsive method of accomplishing this, particularly if the pump supplies a flow rate to a large array of devices. The alternative explored here is placing a dam immediately in front of the channels that could ultimately be controlled automatically in response to flow conditions or chip surface temperature. An adjustable orifice experimental prototype provides a method to seek optimum orifice sizes depending on flow conditions.

2.1.2 Literature Review

Kuan and Kandlikar (2006) used water as the working fluid in rectangular channels of hydraulic diameter (D_h) 0.332 mm (1.054 × 0.197 mm). There were six channels of length 63.5 mm. The heat transfer characteristics of one array without an orifice at each channel inlet were contrasted with an identical array having small inlet orifices drilled at the beginning of each channel. The diameter of each orifice was 0.127 mm, or 6.1% of the channel hydraulic diameter. For a mass flux of 144 kg m^{-2} s^{-1} common between the two setups, it was found that the orifices did not create enough pressure drop to prevent back flow. The difference between inlet pressures for the two cases was only 15 kPa. Surface temperatures were higher for the channels with orifices. For higher mass flux (362.9 kg m^{-2} s^{-1}), the inlet orifices forced an inlet pressure approximately 60 kPa higher than the unrestricted case. The higher inlet pressure caused by the orifices improved heat transfer performance and was shown by lower channel surface temperatures. This indicated that adding a high pressure just upstream of the channel inlets, in addition to increasing mass flux, can produce better heat transfer rates than increasing mass flux alone.

In a study done by Park, Thome, and Michel (2009), refrigerant R134a was passed through an array of 29 channels with dimensions of 30.0 mm × 0.199 mm × 0.756 mm (Length x Width x Depth, D_h of 0.315 mm). The channels were electro-eroded in a copper block. In their test section, results for two different mass fluxes, each with and without orifice, were contrasted. For a high mass flux of 1880 kg m^{-2} s^{-1}, the channels with the orifice in place had a

significantly higher CHF than those without. For the lower mass flux of 390 kg $m^{-2} s^{-1}$ (and thus lower pressure drop across the orifice) no significant difference in CHF was found. The same report included flow visualization results. For the channel geometry described above with an orifice, a flow recirculation pattern established itself within the channels. No backflow beyond the channel inlet was observed. Recirculation occurred with a frequency in the range of 12.5 Hz.

A study by Kosar, Kuo and Peles (2006) showed that it took more heat flux to force the onset of unstable boiling conditions in channels with lengthwise restrictions in place at the inlet of each channel. These restrictions all had the same hydraulic diameter; their length was increased. They found that after a certain length of inlet restriction, no further improvement was made in the heat flux required to cause unstable boiling.

2.1.3 Objectives

This chapter's objectives are threefold: Introduce the test section and cooling loop designs, display data that give proof of the concept of an adjustable orifice for its potential in improving two-phase cooling of electronics, and describe the signal analysis method used to identify oscillations without having pictorial representation of flow patterns. The chapter is split into five main sections: Experimental Setup, Experimental Method, Results, Discussion, and Conclusions.

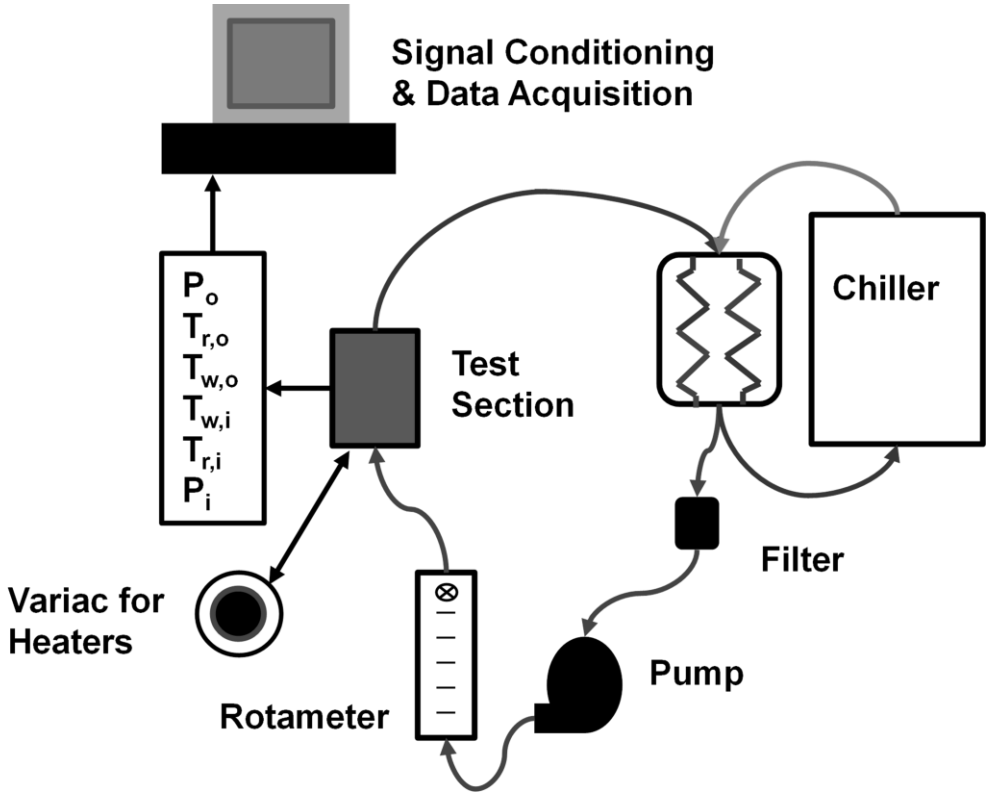

Figure 2.1. Cooling loop schematic.

2.2 Experimental Setup

2.2.1 Flow Loop Configuration

The test section is cooled by a pumped loop containing R134-a, as depicted in Fig. 2.1. The pumped loop has benefits over direct cooling with a vapor compression cycle, to include elimination of the need for superheated vapor at the inlet of a compressor. For a complete discussion about the merits of a pumped loop relative to direct application of a vapor compression cycle, see Phelan et al. (2010). The R134-a exchanges heat in a brazed plate heat exchanger with propylene glycol that has been cooled by the commercial chiller. The commercial chiller is an FTS Maxi-Cool vapor compression chiller that uses R507 with a set

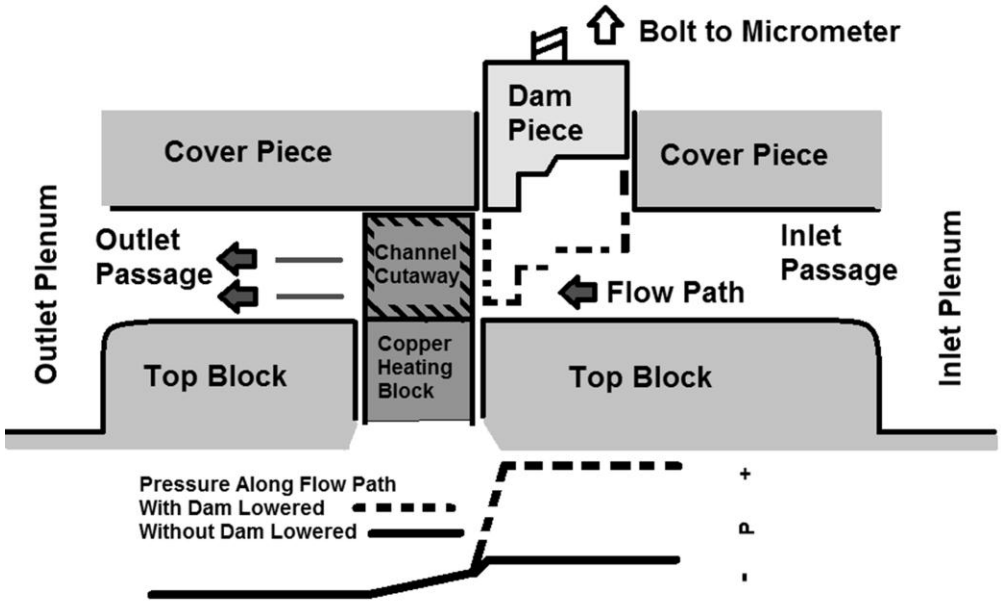

Figure 2.2. Adjustable orifice concept sketch (not to scale).

point capable of maintaining the propylene glycol inlet temperature at ± 0.1 °C under stable conditions. The commercial chiller is cooled by the building water supply. The primary loop is pumped by a positive displacement, pulseless delivery GJ 120 series micro annular gear pump that is magnetically driven. The magnetic drive feature helps avoid damage in the event that the pressure drop in the system is too great for the pump. The pump speed is controlled by a DC power source. Once the pump speed is set, refrigerant mass flow rate to the test section is controlled manually by adjusting the rotameter outlet valve.

2.2.2 Test Section Design

The sketch in Fig. 2.2 is a cutaway view of the assembled inner workings of the test section. It depicts the basic concept of raising and lowering the dam to affect the pressure drop immediately in front of the channels. It shows the flow path of the refrigerant from right to left: in through the inlet passage, under the

dam piece, through the channels, and out through the outlet passage. Figure 2.2 also contains a small pressure vs. position plot that helps explain where the pressure drop increases with reduction in orifice size.

The test section components of interest are labeled in Figure 2.3. The design description is given here from top to bottom, beginning with the micrometer and steel plate combination.

2.2.2.1 Micrometer and steel plate. The micrometer (Fig. 2.3a) is a Swagelok micrometer valve that has an internal bellows that prevents leaking through the micrometer. The micrometer has been modified to provide the control for raising and lowering the dam piece. A 0.64 cm-thick steel plate was welded to the base of the micrometer. On the bottom side of the steel plate is an O-ring (not shown) to provide a seal between it and the cover piece. The O-ring is made of HNBR (hydrogenated nitrile butadiene rubber) which is a standard used in the refrigeration industry with an operating temperature range of -40 °C to 162 °C.

2.2.2.2 Cover and dam. The cover piece (Fig. 2.3b) has a tight fitting hole for the dam piece (Fig. 2.3b or Fig. 2.3e) to slide through. The cover piece is made from the machinable ceramic Rescor 914 and is 2.54 cm thick. This material has a continuous operating temperature of 426 °C (maximum service temperature of 537 °C) and a thermal conductivity of 0.4 W m^{-1} K^{-1}. The dam, which is made from brass, fits right in front of the microchannel inlets upon assembly of the test section.

2.2.2.3 Top block. The top block (Fig. 2.3c) has an O-ring groove on its top surface (shown) and bottom surface that complete the sealing of the test section

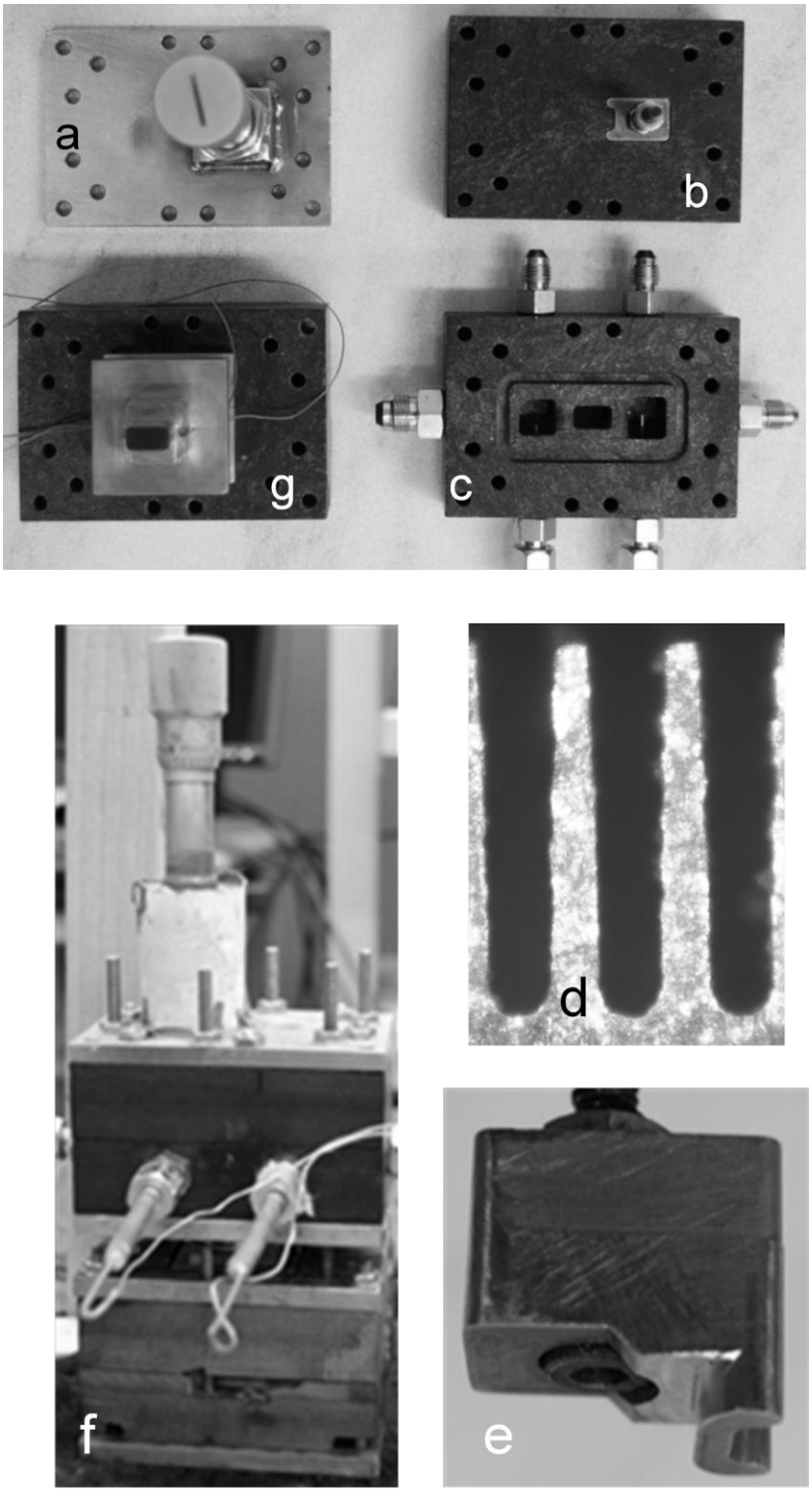

Figure 2.3. Micrometer and steel plate (a), cover and dam (b), top block (c), microchannels (d), dam (e), assembly (f), copper heating block (g).

upon assembly. The top surface O-ring is made of HNBR. The bottom O-ring is made of perflouroelastomer (FFKM). Perflouroelastomer is less stable than HNBR when used with R-134a, but has an operating temperature range of -15 °C to 300 °C. The top block has two ports in both the inlet and outlet plenums for refrigerant temperature and pressure measurement. The fittings shown in Fig. 2.3c have an O-ring face seal to prevent leaking. Fluid leaving the inlet plenum and entering the inlet passage passes over a rounded edge to try to keep the high pressure wall as close to the channel inlets as possible. The fluid then passes through the channels, through the outlet passage, and into the outlet plenum. The hydraulic diameter of the inlet and exit passages is 1.4 mm, and the D_h of the space under the foot of the dam can be varied from 0 to 1.4 mm. The dam slides up and down in front of the channels with less than a 0.05 mm gap between the two features.

2.2.2.4 Copper heating block. The heating block (Fig. 2.3g) is made from Alloy 101 Oxygen Free Copper, and houses four 300 W cartridge heaters in its base. At its top are 31 microchannels (Fig. 2.3d) created using wire electron discharge machining. The channels have an average depth of 0.796 mm, an average width of 0.139 mm, and an average cross sectional area of 0.108 mm^2. The length of each of the channels (at least for the majority of the channels away from the rounded edges of the copper block) is 1.33 cm. The channel D_h was calculated to be 0.245 mm. The channel walls have an average thickness of 0.101 mm.

2.2.2.5 Assembly view and additional notes. See Fig. 2.3f for the assembled test section view. The top of the channels are flush (in the same plane) with the top plane of the top block when assembled. Before any other machining was done to the two pieces, the top of the copper block was machined together with the top block. This ensured a tight fit between the top of the channels and the cover piece once assembled. The top block inlet and exit passage cross sectional area depths and the copper block channel heights are almost the same; the top block inlet and exit channels are 762 μm and the copper block channel heights are 796 μm.

2.2.2.6 Orifice description. There are two orifice descriptions to mention. The first orifice is the gap between the foot of the dam and the bottom of the inlet passage before flow is separated into each individual channel. This orifice D_h can be changed from 0 mm to 1.4 mm. The height of the dam (with the zero reference at the bottom of the inlet passage) can be varied from 0 mm (closed) to 0.762 mm (all the way open) to affect the change in orifice D_h. The second orifice is created for each individual channel by the intersection of the channel walls, the floor of the inlet passage, and the bottom of the dam. If considering the latter definition, the design allows for the individual channel orifice D_h to be varied from 0 mm to 0.235 mm. It is the former definition that will be used for reference when the word orifice is mentioned in the remainder of this paper.

2.2.3 Measurements and Uncertainty

The pressure drop across the test section is measured by subtracting the difference between two pressure transducers measuring static pressure in the inlet and outlet plena of the test section. The transducers' response time is less than 1

ms and accuracy is ± 3.4 kPa for the inlet pressure transducer and ± 8.6 kPa for the outlet pressure transducer (0.25% of full scale).

The wall temperature of the inlet and exit are approximated by two 36 gauge thermocouples placed beneath both locations. A channel 3.18 mm wide and 3.18 mm deep was machined in the copper just below the inlet and outlet of the microchannel array. The two thermocouples in each location were first coated with epoxy over their tips and then set in place. Their actual placement distance from the base of the channels is 2.2 ± 0.2 mm. Due to the wall temperature thermocouple location, their readings give an estimate of the temperatures at the base of the inlet and outlet of the microchannels and an indication of wall temperature rise from inlet to outlet. The inlet and outlet refrigerant temperatures are measured in the respective plenums by one probe type thermocouple in each location. All thermocouples are T type. They were calibrated in a constant temperature bath, and uncertainty in temperature measurements is estimated to be ± 0.5 °C. There are four Variac-controlled 300 W cartridge heaters that were coated with high-temperature thermal paste and placed in the base of the copper block. The current and voltage for the heaters were in phase and thus power was measured by multiplying voltage drop across the heaters with the current flow through the heaters. Current was found by measuring the voltage drop across a shunt placed in series with the heaters. Total uncertainty in the power supplied to the test section is estimated to be ±5.5%, and the uncertainty in the heat flux measurement to be ±5.8%, but with additional uncertainty from heat losses. Heat

loss estimation is described in a separate section. The data from each instrument are monitored by a National Instruments data acquisition system.

Flow rate is measured by a Kings Instrument 7430 Low-flow Rotameter with accuracy of ± 4 % of full scale flow. At 0 °C, the full scale flow for R134a is 9.9 g s^{-1}, therefore accuracy is ± 0.4 g s^{-1}, and repeatability is 1%. This may cause alarm as flow rates were as low as 1 g s^{-1}; however, during experimentation, repeatability was more important than accuracy for comparing different dam heights.

2.2.4 Addressing Thermocouple Response

The wall temperature thermocouple locations (2 mm below the base of the microchannels) are positioned well to register wall temperature oscillations at the base of the microchannels. A first approximation for what the thermocouples' gains are can be made using a simplified model of the very top portion of the copper block.

In this simple model, each wall temperature thermocouple is assumed to be massless with an ideal response (i.e. a perfect amplification ratio, or gain of 1) when imbedded in the copper block just below the channels. An imaginary thin slice off the top of the copper block immediately beneath the channels and with a 2 mm depth is used as a volume (*V)* estimate. The heat transfer coefficient, *h*, is assumed to stay constant during the course of an oscillation. The time constant is estimated as (Incropera & DeWitt, 1996)

$$\tau = \frac{\rho V c}{h A_s} \tag{1.1}$$

where ρ is the copper block density, c the heat capacity of copper, and A_s the surface area exposed to convection. Using an estimation for h of 70000 W m^{-2} °C^{-1} based on average wall and refrigerant temperatures for steady state conditions at 300 kg m^{-2} s^{-1} mass flux, $\tau \cong 0.00002$ s. This time constant is smaller than that of the pressure sensors used (which have a time constant of 0.0006 s).

With this τ value, the gain at a given frequency, $G(f)$, can be calculated (Beckwith, Marangoni, & Lienhard, 1993). The maximum temperature the thermocouple junction would reach if the driving temperature difference was to stay at its maximum rather than oscillate is T_m. The maximum temperature actually seen at the thermocouple junction is T_{act}. With these definitions established,

$$G(f) = \frac{T_{act}}{T_m} = \frac{1}{\sqrt{1 + (2\pi f\tau)^2}} \tag{1.2}$$

and the resulting gain for the thermocouples is nearly perfect (perfect gain is equal to 1) for the range of frequencies considered. Thus, there is no necessity for correcting the peak amplitudes in the following fast Fourier transform (FFT) plots due to errors imposed by response time.

2.2.5 Heat Losses

Heat losses were estimated by developing a plot that showed the linear relationship between mid-copper block temperature and heat loss. Data for the plot were obtained by applying a known power input to the test section empty of refrigerant and measuring the surface temperature at the middle of the copper

block once steady state was reached (6 hours was allowed to pass). This was done for several known power inputs and then a plot was made of mid-copper block temperature vs. heat loss. Heat flux data could be corrected afterwards. Room temperature stayed at 22 °C ± 2 °C during experimentation, so the heat loss calibration remained applicable throughout testing.

2.2.6 Identifying Steady State

To estimate arrival at steady state conditions, a three-time-constant approach was taken. Once three time constants have passed for an object being heated, it is within five percent of its final temperature, assuming a simple first-order (lumped capacitance) system. Immediately upon applying power to the heaters in the test section, the first 20 seconds of mid-copper block temperatures were averaged. Thereafter, a continuously updating 20 second average was kept. Once it decayed to 37 % of the first 20 second average, one time constant was considered to have been reached. For two time constants, the 20 second average would be 14% of the original. For three time constants, the 20 second average would be 5% of the original. As the same instrument was used to measure temperature, bias errors were not an issue. Averaging reduced precision errors. From this procedure, one hour and fifteen minutes was ample time (more than three time constants) for steady state to be reached for the initial large step input in the 300 kg m^{-2} s^{-1} and 600 kg m^{-2} s^{-1} experimental runs.

2.3 Experimental Method

Experiments were conducted with mass fluxes of 300 kg m^{-2} s^{-1} and 600 kg m^{-2} s^{-1}. Nine different orifice sizes were tested for each mass flux. The

power input was set at a point which ensured boiling for much of the channel length once steady-state conditions were reached. For all experimental runs, the inlet conditions were saturated liquid, or sufficiently close so that the enthalpy change to reach saturation was negligible. This means that the refrigerant would begin to boil shortly after entering the channels. The test section was allowed to come to steady state for one hour and fifteen minutes with the orifice D_h at its largest setting. Two minutes of data were taken with the orifice wide open. The orifice was then reduced to the next smaller size, ten minutes were allowed to pass, and two more minutes of data were taken. This process was repeated through the smallest orifice D_h possible, 0.025 mm, before the dam bottomed out. The smallest orifice size was 1.7% of the largest setting. The sample frequency for each two-minute record of data was 110 samples per second. This sample rate resolved frequencies as high as 55 Hz. The frequencies at which significant peaks occurred were 1 Hz and then in the range of 6 to 12 Hz, so this sample rate was a good choice.

2.4 Results

2.4.1 Wall Temperature Comparison between Large and Small Orifice Size

One effect the orifice size has on cooling performance is indicated in the temperatures recorded by the inlet and outlet wall thermocouples. Averaging the two provides an estimate for average wall temperature at the base of the channels. Figure 4 shows the average wall temperature reached for each orifice size at steady-state conditions with a 300 kg m^{-2} s^{-1} mass flux. Figure 2.5 shows the same for a 600 kg m^{-2} s^{-1} mass flux. Each data point displayed is an average of the full

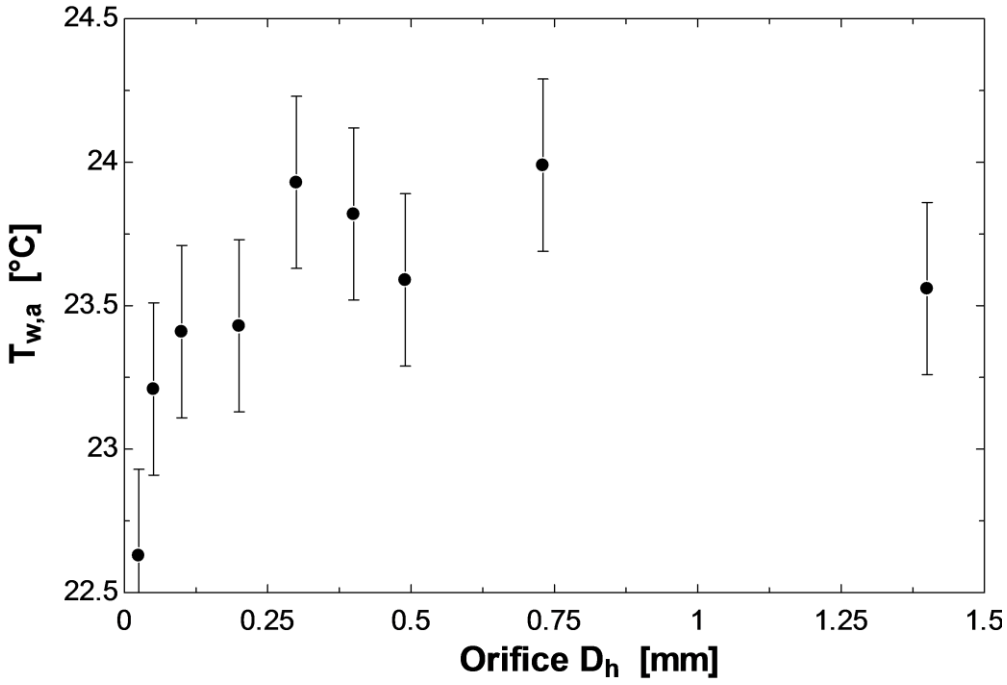

Figure 2.4. Average of inlet and outlet wall temperatures for different orifice sizes under steady state conditions, 300 kg m^{-2} s^{-1} mass flux, and heat flux = 178 W cm^{-2}.

two minutes of data for the associated orifice D_h. The trend in average wall temperatures is very similar for both mass fluxes considered. If the dam is closed slightly, hardly any pressure drop is created but downstream flow is disrupted in a fashion that actually reduces the heat transfer coefficient and increases the average wall temperature.

As the orifice closes further, the wall temperature trend is reversed and lower temperatures are seen. This is explained by either vapor production or temperature drop in the liquid in accordance with its Joule-Thompson coefficient. The other resulting benefit is a reduction in oscillation amplitudes, which can be shown

through frequency analysis. A brief look at time domain outlet wall temperature data for the 300 kg m^{-2} s^{-1} and 600 kg m^{-2} s^{-1} mass flux experiments provides an introduction to the frequency analysis discussed in the next section.

Figure 2.6 shows time domain data for a 300 kg m^{-2} s^{-1} mass flux at two orifice sizes, D_h = 1.4 mm and D_h = 0.025 mm. Figure 2.7 shows the same for a mass flux of 600 kg m^{-2} s^{-1}. It is much easier to identify the 1 Hz oscillations with the larger mass flux and higher heat flux represented in Fig. 2.7; however, it is difficult at the resolution shown in the plot to see that there is also a secondary significant oscillation occurring at a frequency of 10 Hz. This is where frequency

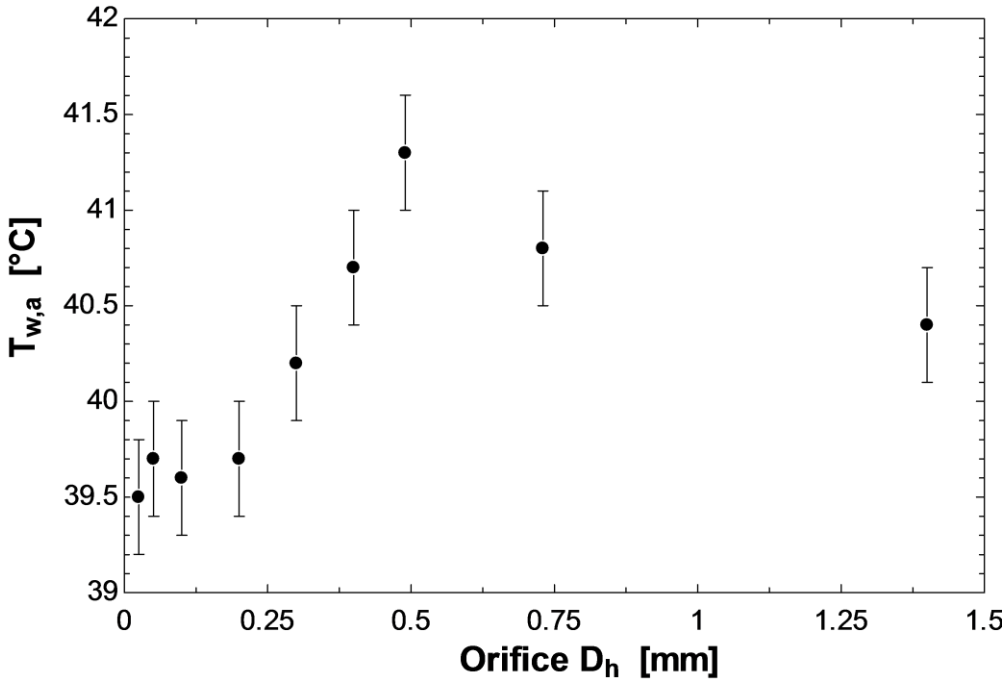

Figure 2.5. Average of inlet and outlet wall temperatures for different orifice sizes under steady state conditions, 600 kg m^{-2} s^{-1} mass flux, and heat flux = 337 W cm^{-2}.

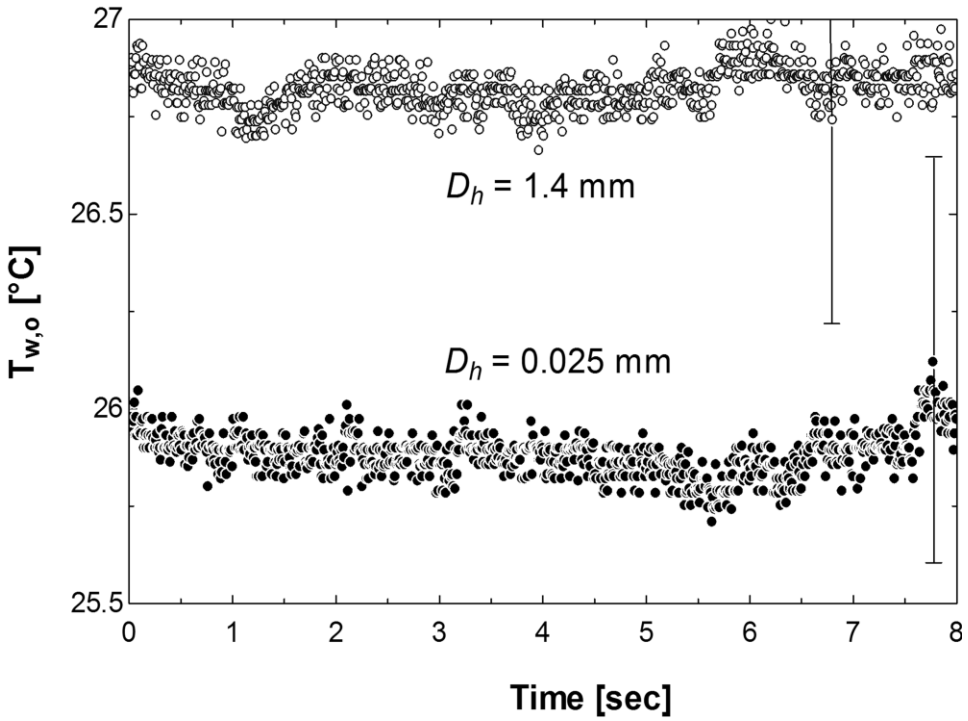

Figure 2.6. Representative time domain comparison for 300 kg m^{-2} s^{-1} mass flux.

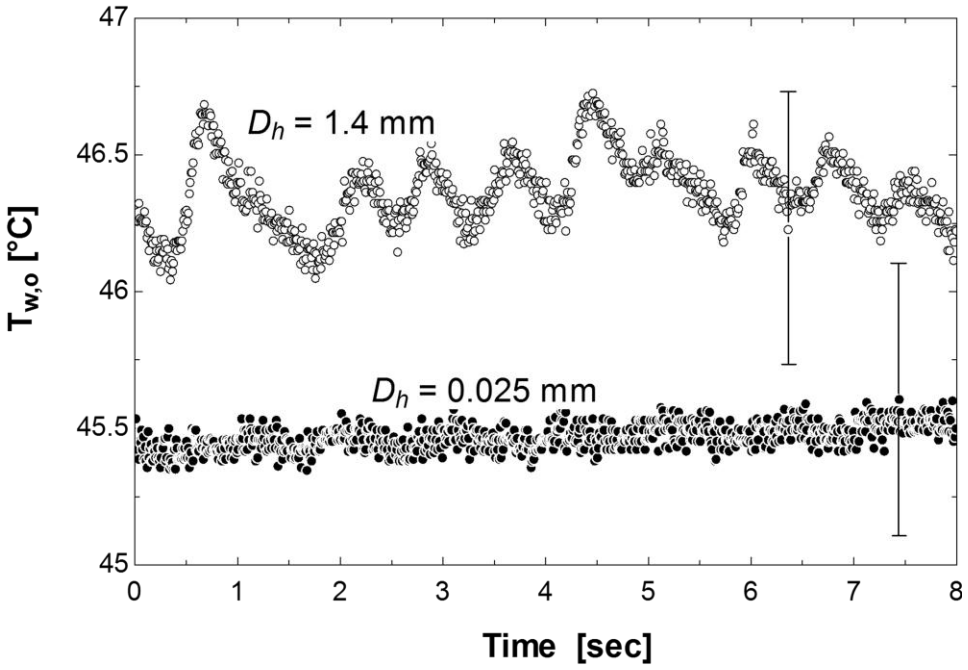

Figure 2.7. Representative time domain comparison for 600 kg m^{-2} s^{-1} mass flux.

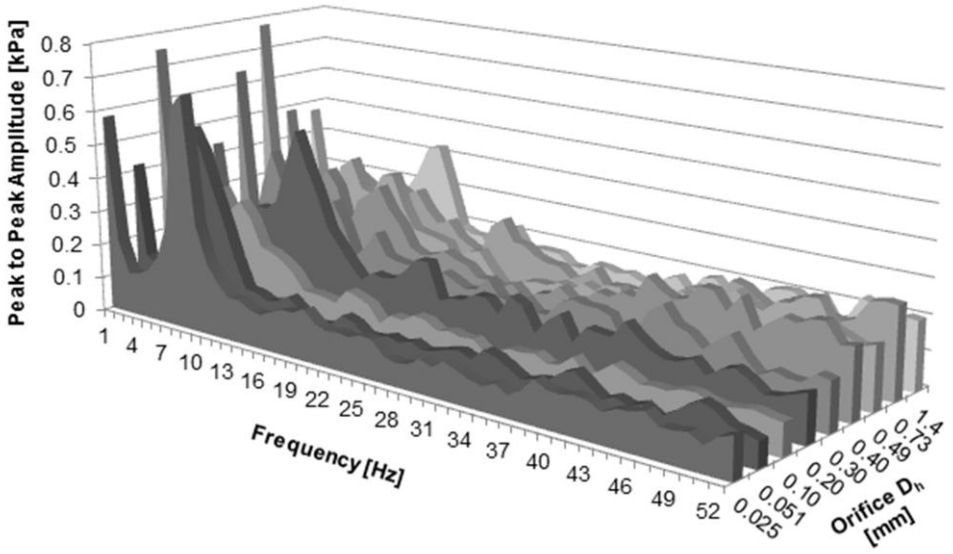

Figure 2.8. Inlet pressure FFT results, 300 kg m^{-2} s^{-1} mass flux, heat flux = 178 W cm^{-2}.

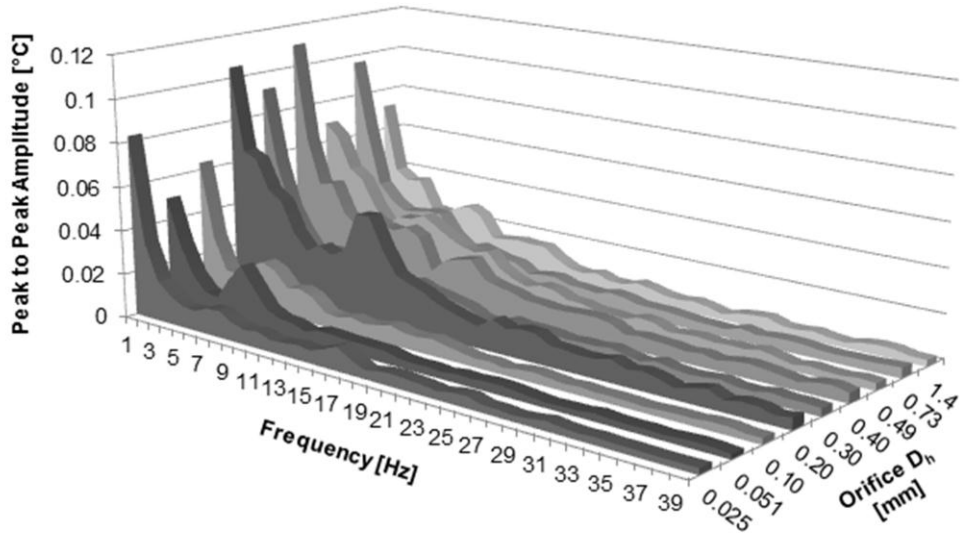

Figure 2.9. Outlet wall temperature FFT results, 300 kg m^{-2} s^{-1} mass flux, heat flux = 178 W cm^{-2}.

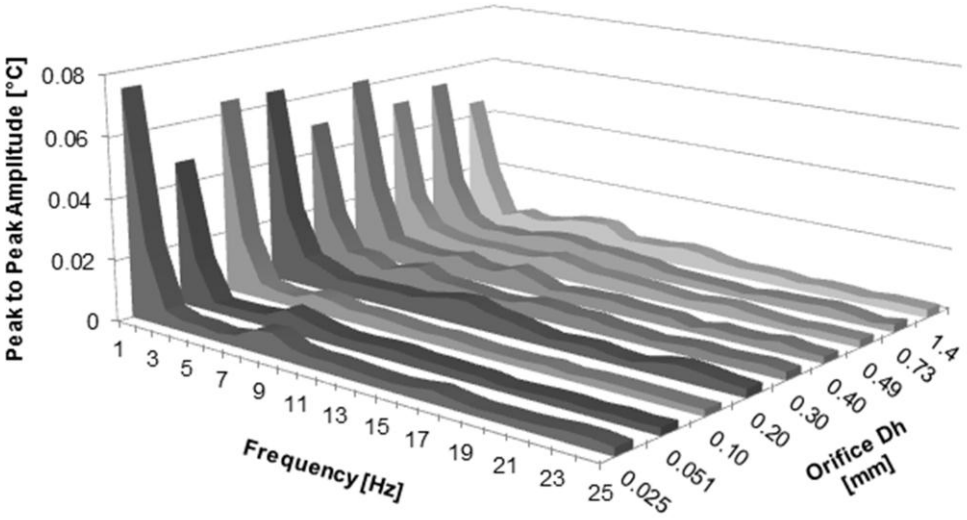

Figure 2.10. Inlet wall temperature FFT results, 300 kg m^{-2} s^{-1} mass flux, heat flux = 178 W cm^{-2}.

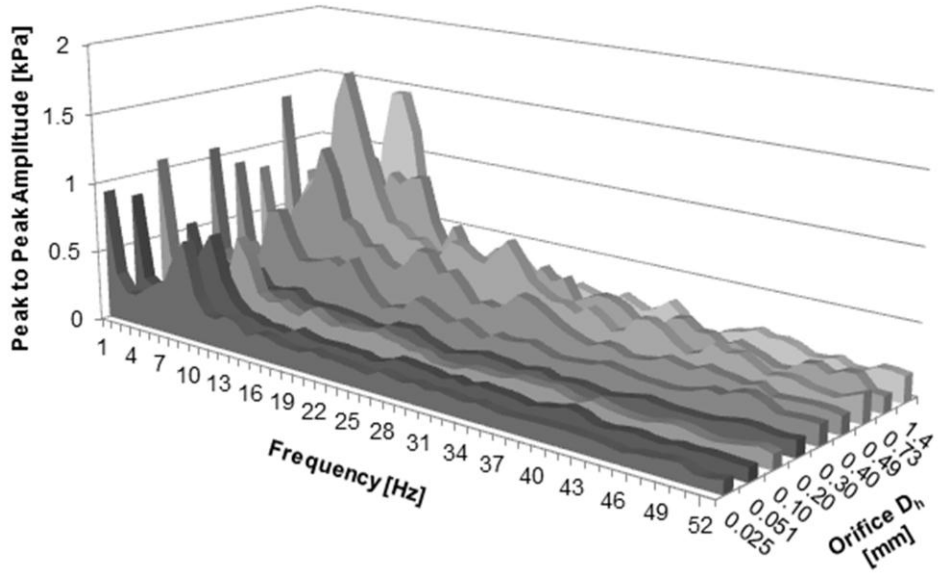

Figure 2.11. Inlet pressure FFT results, 600 kg m^{-2} s^{-1} mass flux, heat flux = 337 W cm^{-2}.

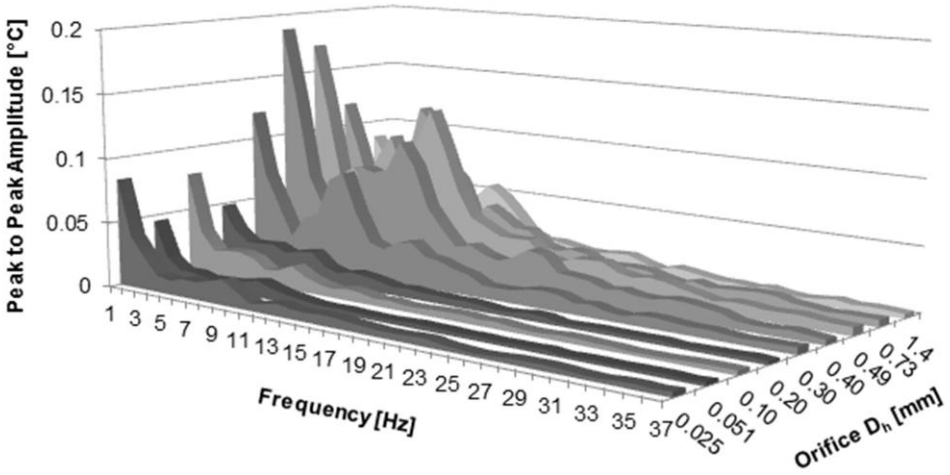

Figure 2.12. Outlet wall temperature FFT results, 600 kg m^{-2} s^{-1} mass flux, heat flux = 337 W cm^{-2}.

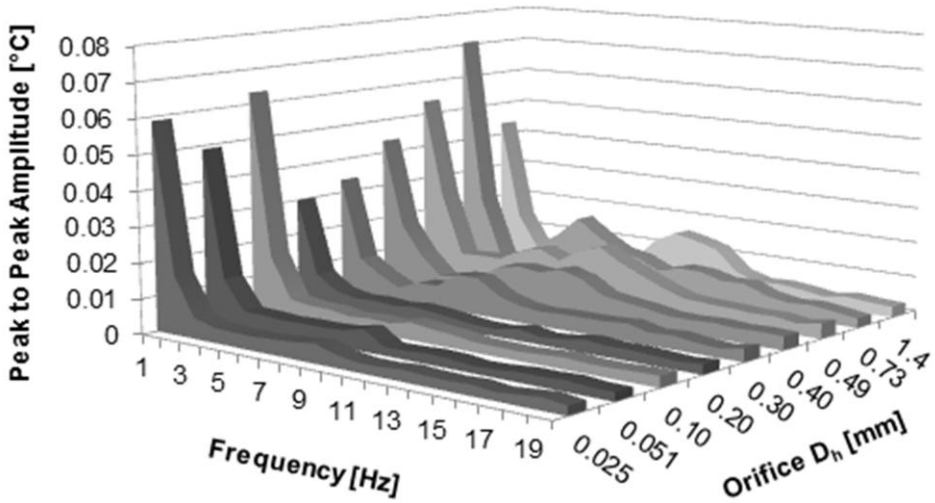

Figure 2.13. Inlet wall temperature FFT results, 600 kg m^{-2} s^{-1} mass flux, heat flux = 337 W cm^{-2}.

analysis can give indication of what is happening inside the channels when pictorial representation is not possible.

2.4.2 Assessing Design Effectiveness through Frequency Analysis

Using the fast Fourier transform, it is possible to assess how well different orifice sizes control oscillations under the two mass fluxes and heat fluxes considered. A brief description of how the signal analysis was conducted follows. For both mass fluxes considered, the frequency spectra of inlet pressure sensor, outlet wall temperature thermocouple, and inlet wall temperature thermocouple were plotted in Figs. 2.8-2.13. The frequency domain data for these figures were obtained by processing time domain data through code that made use of Matlab's Fast Fourier Transform function. A Hanning Window was applied to each set of 2 minutes of steady-state time domain data associated with a given orifice size and heat flux before processing. The Hanning Window is a good window to use initially when processing data with an FFT algorithm as it provides a balance of minimizing spectral leakage and maintaining frequency resolution in the resulting frequency domain plots (Lynn, 1998). The zero hertz frequency was eliminated by taking the average of each data set and subtracting the result from each point in the data. This is important to do because the zero hertz frequency represents the average output from the sensor in question. In other words, if there were no noise and separate frequencies making up the output signal from the sensor, the zero hertz amplitude would be the value the experimentalist reports as the pressure or temperature at the time of measurement.

Table 2.1. Correlation coefficients between average wall temperatures and associated oscillation amplitudes for 300 kg m^{-2} s^{-1} mass flux.

300 KG M^{-2} S^{-1} MASS FLUX									
Orifice Dh [mm]	0.025	0.051	0.10	0.20	0.30	0.40	0.49	0.73	1.4
Average Wall Temperature $T_{w,a}$ [°C]	22.6	23.2	23.4	23.4	23.9	23.8	23.6	24.0	23.6
INLET PRESSURE (Refer to Fig. 4 and Fig. 8)									
Frequency of Initial Peak (always 1 Hz)	1	1	1	1	1	1	1	1	1
Initial Peak Amplitude [kPa]	0.58	0.42	0.75	0.33	0.43	0.64	0.77	0.48	0.47
Correlation Coefficient Between Initial Peak Amplitudes and $T_{w,a}$	-0.06								
Frequency of Secondary Peak [Hz]	9	7	7	12	7	10	10	11	14
Secondary Peak Amplitude [kPa]	0.69	0.56	0.37	0.55	0.44	0.39	0.40	0.33	0.42
Correlation Coefficient Between Secondary Peak Amplitude and $T_{w,a}$	-0.85								
OUTLET WALL TEMPERATURE (Refer to Fig. 4 and Fig. 9)									
Frequency of Initial Peak (always 1 Hz)	1	1	1	1	1	1	1	1	1
Initial Peak Amplitude [°C]	0.083	0.050	0.063	0.105	0.092	0.110	0.069	0.096	0.071
Correlation Coefficient Between Initial Peak Amplitudes and $T_{w,a}$	0.41								
Frequency of Secondary Peak [Hz]	8	7	6	12	10	7	9	7	8
Secondary Peak Amplitude [°C]	0.012	0.027	0.023	0.048	0.022	0.034	0.033	0.029	0.028
Correlation Coefficient Between Secondary Peak Amplitude and $T_{w,a}$	0.40								
INLET WALL TEMPERATURE (Refer to Fig. 4 and Fig. 10)									
Frequency of Initial Peak (always 1 Hz)	1	1	1	1	1	1	1	1	1
Initial Peak Amplitude [°C]	0.075	0.047	0.064	0.064	0.050	0.062	0.051	0.054	0.045
Correlation Coefficient Between Initial Peak Amplitudes and $T_{w,a}$	-0.54								
Frequency of Secondary Peak [Hz]	9	7	6	12	7	7	10	8	9
Secondary Peak Amplitude [°C]	0.0079	0.0073	0.0061	0.0084	0.0079	0.0076	0.0074	0.0074	0.0089
Correlation Coefficient Between Secondary Peak Amplitude and $T_{w,a}$	-0.02								

Table 2.2. Correlation coefficients between average wall temperatures and associated oscillation amplitudes for 600 kg m^{-2} s^{-1} mass flux.

600 KG M^{-2} S^{-1} MASS FLUX									
Orifice Dh [mm]	0.025	0.051	0.10	0.20	0.30	0.40	0.49	0.73	1.4
Average Wall Temperature $T_{w,a}$ [°C]	39.5	39.7	39.6	39.7	40.2	40.7	41.3	40.8	40.4
INLET PRESSURE (Refer to Fig. 5 and Fig. 11)									
Frequency of Initial Peak (always 1 Hz)	1	1	1	1	1	1	1	1	1
Initial Peak Amplitude [kPa]	0.93	0.85	1.07	0.54	1.07	0.91	0.84	1.35	0.72
Correlation Coefficient Between Initial Peak Amplitudes and $T_{w,a}$	0.21								
Frequency of Secondary Peak [Hz]	9	9	9	8	8	10	10	7	11
Secondary Peak Amplitude [kPa]	0.70	0.69	0.62	0.31	0.71	1.16	1.68	1.47	1.46
Correlation Coefficient Between Secondary Peak Amplitude and $T_{w,a}$	0.89								
OUTLET WALL TEMPERATURE (Refer to Fig. 5 and Fig. 12)									
Frequency of Initial Peak (always 1 Hz)	1	1	1	1	1	1	1	1	1
Initial Peak Amplitude [°C]	0.083	0.045	0.079	0.049	0.12	0.19	0.17	0.12	0.09
Correlation Coefficient Between 1 [Hz] Amplitudes and $T_{w,a}$	0.83								
Frequency of Secondary Peak [Hz]	9	9	5	5	8	10	10	7	10
Secondary Peak Amplitude [°C]	0.020	0.013	0.022	0.023	0.081	0.10	0.13	0.12	0.06
Correlation Coefficient Between Secondary Peak Amplitude and $T_{w,a}$	0.95								
INLET WALL TEMPERATURE (Refer to Fig. 5 and Fig. 13)									
Frequency of Initial Peak (always 1 Hz)	1	1	1	1	1	1	1	1	1
Initial Peak Amplitude [°C]	0.059	0.049	0.063	0.030	0.034	0.044	0.054	0.071	0.043
Correlation Coefficient Between 1 [Hz] Amplitudes and $T_{w,a}$	0.12								
Frequency of Secondary Peak [Hz]	9	9	9	8	8	10	10	7	11
Secondary Peak Amplitude [°C]	0.0055	0.0062	0.0050	0.0042	0.011	0.012	0.016	0.020	0.016
Correlation Coefficient Between Secondary Peak Amplitude and $T_{w,a}$	0.89								

Use of the Hanning Window halves the magnitude of the amplitudes output from the FFT algorithm, and this was accounted for before plotting. Location of a sensor was important in its ability to identify oscillations. The three sensors mentioned above proved reliable for providing evidence of frequencies with large amplitudes present in their signals. The inlet refrigerant thermocouple was too far upstream to register temperature oscillations caused by backflow or bubbles moving upstream momentarily. The outlet pressure sensor and outlet refrigerant side thermocouple were exposed to a large amount of vapor, likely damping oscillations present. These last two sensors would also have been subject to any condensate in the downstream tube of the cooling loop.

Each of the frequency domain plots in Figures 2.8-2.13 contains 9 rows of frequency domain data, corresponding to the 9 different orifice sizes tested. The depth axis indicates the orifice size associated with each set of frequency data, and this number increases from front to back of the plot. The vertical axis indicates peak-to-peak magnitude in appropriate units of measure. The horizontal axis indicates frequency in units of Hertz.

It is not possible to discern a clear pattern of improvement in oscillation control with varying orifice size by looking at the 300 kg m^{-2} s^{-1} plots in Figs. 2.8-2.10. For 600 kg m^{-2} s^{-1} mass flux, Figs. 2.11-2.13 showed a distinct impact on oscillation amplitude in response to orifice size. These findings are in good keeping with the Kuan and Kandlikar (2006) study mentioned in the Literature Review. Their study indicated a threshold of orifice induced pressure drop beyond which there is improved heat transfer and reduction of oscillations. For a

600 kg m^{-2} s^{-1} mass flux, there is a certain orifice size above which improvement is minimal or possibly worse than wide open flow, but below which both wall temperature and oscillation amplitude decrease. For a 600 kg m^{-2} s^{-1} mass flux, the first orifice D_h that showed an appreciable improvement in inlet pressure oscillation amplitude was 14% of the D_h for a wide open orifice. It is fairly easy to visually determine how the major peaks seen in Figs. 2.11-2.13 correlate to the average wall temperatures shown in Fig. 2.5. It is not possible to do the same with the 300 kg m^{-2} s^{-1} waterfall plots, Figs. 2.6-2.8, and the average wall temperatures shown in Fig. 4. Tables 2.1 and 2.2 are included to show correlations between variables. For a 600 kg m^{-2} s^{-1} mass flux, there is strong correlation between the average wall temperatures shown in Fig. 2.5 and the highest peak to peak amplitudes for frequencies in the range of 5 to 11 Hz. The relatively high values for the amplitudes at the 1 Hz frequency seen throughout all six of the waterfall plots showed very low correlation coefficients when compared to the average wall temperatures.

2.5 Discussion

The correlation coefficients in Table 2.2 show that as peak-to-peak amplitudes increased in the 600 kg m^{-2} s^{-1} mass flux results, so did average wall temperatures. This was not the case for the 300 kg m^{-2} s^{-1} mass flux, as shown in Table 2.1. Smaller orifices created less pressure drop before the channels than in the 600 kg m^{-2} s^{-1} mass flux experiments and had no significant impact on oscillations. For the 300 kg m^{-2} s^{-1} case, oscillations were all ready of small amplitude with a

wide open orifice. Taken alone, the 600 kg m^{-2} s^{-1} mass flux observations would indicate that the wall temperature decrease with smaller orifice size is caused by oscillation reduction. The 300 kg m^{-2} s^{-1} correlation coefficients indicate that there is another reason for wall temperature reduction with smaller orifice size. Since the smaller orifice sizes had similar effects on wall temperatures for both flow rates, the wall temperature cooling is due to the cooling of the refrigerant associated with a drop in pressure.

2.6 Conclusion

The concept of a controllable inlet orifice is useful for slight reductions in wall temperatures at very low mass fluxes in a pumped loop when cooling with R134-a. Also, as the mass flux is increased from 300 kg m^{-2} s^{-1} to 600 kg m^{-2} s^{-1} and heat flux increases commensurately, oscillations become significant and are damped effectively by reducing the orifice size.

Consistent and sharply defined oscillations do not occur under the 300 kg m^{-2} s^{-1} mass flux flow conditions, but they do for 600 kg m^{-2} s^{-1} mass flux flow conditions. Both mass fluxes experience similar wall temperature drops of approximately 1 °C with orifice size reduction. These wall temperature drops occur very rapidly as the increased pressure drop is placed in front of the channels. It is concluded that at low flow rates, it is not the result of oscillation damping that improves wall temperatures. Instead it is the Joule-Thompson effect that occurs when a large pressure drop is created in front of the channels. The adage ‘correlation does not mean causation’ applies. As critical heat flux is approached, the damping effect should become more important and a correlation

between oscillation amplitudes and critical heat flux values may be shown to be valid. There may be a tradeoff between how much cooling occurs through the Joule-Thompson effect and reduction in capacity, i.e. if the pressure drop is great enough to cause vapor to appear, some loss in cooling capacity occurs.

It is possible to assess the success of a design at mitigating oscillations without recording images of the actual flow in microchannels. Flow visualization has the benefits of high fidelity regarding flow patterns, but frequency analysis can give a measure of the strength of the forcing functions causing certain frequencies of oscillation. This means that future work in which a device for orifice size control interferes with flow visualization can be done with higher confidence in being able to draw out necessary information from the sensors.

Chapter 3: Heat Sink Effect on System Pressure and Mass Flow Rate in a Pumped Refrigerant Loop

Abstract

Pumped refrigerant loops (PRL) which are aimed at eventually cooling electronics often reject heat to a vapor compression cycle. A vapor compression cycle (VCC) uses a proportional, integral, and derivative controller to maintain desired conditions in its evaporator. These controllers apply an algorithm that has an associated time response. This time response and constant adjustment of the expansion valve in the VCC can result in rapid deviations from the set point temperature for the evaporator. When a PRL is coupled to a VCC, the result in the PRL can often be rapid system-wide changes in pressure and mass flow rate. Three options for removing heat from the PRL were evaluated for their effect on PRL system pressure and mass flow rate. Two of the options were variations of the direct coupling option, while the third eliminated the direct coupling to a VCC and used an ice water heat sink in its place. Rejecting heat from a PRL to an ice water heat sink provided more stable system pressures and mass flow rates and less of a propensity for premature dry out than rejecting heat directly to a vapor compression cycle (VCC). The PRL priming time required when coupled to an ice water heat sink can occur in seconds rather than the minutes required when the PRL is directly coupled to a VCC. For certain operating conditions in which thermal storage can be taken advantage of, the ice water heat sink also provides an opportunity for electricity usage cost savings of 10 percent or more over using the VCC alone. To remove heat from the refrigerant in a PRL, an ice water heat

sink has a number of potential advantages over a directly coupled VCC. It provides very stable condensing conditions and thus mass flow rates, and it has potential maintenance and electricity cost savings over a tightly controlled VCC.

3.1 Introduction

3.1.1 Motivation

During experimentation to determine the effect of an adjustable inlet orifice on instabilities in microchannels (Odom et al., 2011), it was found that rapid deviations in the range of one to three degrees Celsius from the vapor compression cycle's (VCC) set point temperature caused variations in the mass flow rate in the pumped refrigerant loop (PRL). A rotameter was used to measure the mass flow rate in the experiments, so it was possible to watch the rotameter float vary its position in harmony with the vapor compression cycle's proportional, integral, and derivative (PID) controller's attempts to maintain the desired set point temperature. These deviations were managed effectively by monitoring the flow rate and adjusting the power input to the pump in the PRL for lower heat flux experiments; however, during the course of critical heat flux (CHF) data collection, it was recognized that the problem was causing premature dry out, or early onset of CHF. Manual correction of the mass flow rate had to occur almost continuously and was not enough to counteract the effects of changes in system pressure. This prompted experimentation to find a better solution for removing heat from the PRL without purchasing a more complex and expensive chiller.

3.1.2 Background

Temperature has a major impact on the life expectancy of an electronics package. Concerns include both the temperature magnitude and temperature cycling amplitude to which the materials within the electronics package are exposed (Ulrich & Brown, 2006). For perspective and simplicity, an electronics package will be defined here as an integrated circuit along with its casing and leads; however, the ideas presented can be applied to any electronics device thermal management problem where the PRL is a viable cooling method. Faster and faster chip speeds mean greater heat production and thus a higher requirement for heat removal (Ulrich & Brown). Refrigerated cooling of electronics makes the faster switching speeds and handling of the higher heat generation possible (Kirschman, 1985). Refrigerants can be boiled at very low temperatures before requiring vacuum. Thus, a pumped loop using refrigerant as the working fluid can keep chip surface temperatures very low while simultaneously removing large amounts of heat. As an indicator of what the future holds with regards to chip cooling requirements, the Office of Naval Research has set a goal for its supported researchers of obtaining 1000 W cm^{-2} of cooling while maintaining chip surface temperatures below 60 °C.

Jaeseon Lee and Issam Mudawar (2008) have advocated using the PRL as the primary cooling loop in contact with the device to be cooled. They have described performance differences between directly cooling an electronic device with a pumped loop and directly cooling with a vapor compression cycle (VCC), using R-134a as the cooling fluid in both cases (Lee & Mudawar, 2009). For the latter

option, the microchannels removing heat from the electronic device functioned as the VCC evaporator. In order to supply the needed superheated vapor to the compressor, mainly high void fraction saturated flow had to occur in the microchannels. In the pumped loop, low void fraction subcooled boiling conditions could be maintained. In either subcooled or saturated boiling, the benefits of the high heat transfer coefficients and constant refrigerant temperatures associated with using the latent heat of vaporization are ideal for electronics cooling (Lee & Mudawar, 2005). Boiling that occurs in lower quality ranges has much higher heat transfer coefficients than boiling in higher quality ranges (Lee & Mudawar). Phelan et al. (2010) found the pumped loop to be a more optimal solution in terms of energy savings than the direct cooling method as well. An article written by Jie Liu and Kaihua Guo (2010) described the evaluation of a PRL's potential to cool multiple evaporators in a space environment using CO_2 as the working fluid. Their experimental test setup had much longer lengths of tubing between components than in the present study, and thus experienced long system startup times nearing half an hour. Despite the lengthy start up times, they found the PRL to be capable of handling transient loads. All of the studies mentioned here are in favor of the PRL for removing heat from electronics; this paper addresses how to best remove heat from the refrigerant in the PRL.

A pumped refrigerant loop typically rejects heat directly to a VCC's refrigerant through heat exchange in the VCC's evaporator or through an intermediate process fluid between the VCC and the PRL (Lee & Mudawar, 2008;

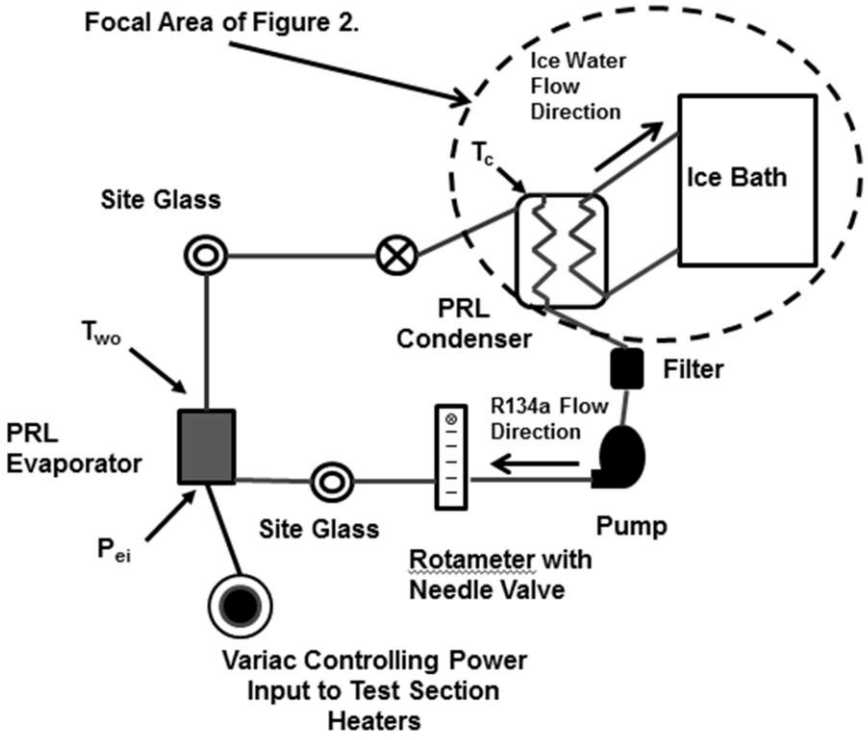

Figure 3.1. Pumped refrigerant loop (PRL) schematic.

Park, Thome, & Michel, 2009). The objective here is to describe the potential difficulties in using a VCC directly coupled to a PRL in this fashion, and show data that prove the benefits of coupling the PRL to a pumped ice water heat sink instead. Three different heat rejection setups were evaluated before reaching the conclusion that a pumped ice water heat sink with a VCC making the ice is a better option than direct coupling of the PRL to a VCC. Figure 3.1 is the PRL built and used to evaluate differences among the three setups. The dashed circle in the figure indicates the portion of the loop that was changed during the three different setups, and their differences will be discussed further in the experimental

setup and results sections. The remaining sections of the paper are refrigerant behavior, vapor compression PID tuning and its drawbacks, experimental setup, method, results, and conclusions.

3.2 Refrigerant Behavior

With refrigerants, slight changes in temperature can cause significant changes in the pressure of a closed system. For instance, the difference in pressure between saturated R-134a at 0 °C and 2 °C is 21.8 kPa (For 0 to 0.5 °C, the difference is 5.4 kPa or 0.78 psi). These differences in pressure are termed significant primarily because they can rapidly change conditions at a point in the pumped loop from slightly subcooled to saturated or superheated. It is preferred that the only condition-changing force in the evaporator comes from an increase in heat flux from the device being cooled. A basic course in thermodynamics will discuss steady-state performance of individual components of a system. How one component affects the entire system's operating conditions is rarely mentioned. To understand how refrigerant behaves on a system level with multiple components in series like a PRL, it is best to first review how refrigerant behaves in a tank at room temperature. Then the refrigerant behavior in a pumped loop will be considered.

3.2.1 Stationary Tank

The pressure in a tank of refrigerant sitting with its contents at uniform room temperature throughout will be the saturation pressure for the refrigerant at room temperature. It does not matter if there is a little bit of refrigerant in the tank or a lot, the pressure will be the same in both cases. More generally defined, the

pressure in the tank is determined from the vapor pressure at the liquid surface. This vapor pressure is the refrigerant's saturation pressure corresponding to the surface temperature of the liquid (Çengel & Boles, 2008).

The next example to consider as background to understanding the pumped loop is when a stationary tank at room temperature is used to charge a refrigerant system. The refrigerant system is cold and at low pressure, while the refrigerant in the tank is warm and at a higher pressure. The two are connected and a valve is opened between them. The refrigerant in the can will begin to pass refrigerant to the system to be charged. If the tank has its valve at the bottom, liquid refrigerant will be forced to flow to the refrigerant system. If the tank has its valve at the top, vapor will begin to flow to the refrigerant system. In either case, the pressure in the tank drops, and as it does so, vapor begins to be produced. As vapor is produced, the liquid remaining in the tank will begin to cool, but it will have a temperature gradient between its high and low points. In this same fashion, the liquid in a condenser will have a temperature gradient between the liquid closer to its top and the liquid leaving the bottom moving towards the pump. The liquid at the bottom of the condenser is also at a higher pressure simply due to the weight of liquid above it, thus increasing the amount it is subcooled.

3.2.2 Pumped Loop

In a pumped loop, there is the potential to have several components changing the system pressure at once. An example would be when the condensing temperature is dropping but the evaporator is experiencing an increase in load. The resulting effect on system pressure would be a combination of the effects of

each component. When conditions in an evaporator are two-phase, small drops in system pressure could force superheated, lower heat transfer coefficient conditions to develop. If a load spike from the device being cooled occurred simultaneously, temperatures could elevate out of control. Changes in system pressure affect the volume of vapor produced and position of the start of two-phase conditions, which in turn causes a change to the pressure losses the pump must overcome. The result is mass flow rate fluctuation. Devices being cooled will also experience temperature fluctuations in direct correlation to the magnitude of system pressure changes. Thus, condensing temperature swings are a major concern and will require controlling.

For a VCC, controlling these swings will be accomplished to varying degrees of success by the use of proportional, integral, and derivative (PID) tuning applied to an electronic expansion valve upstream from its evaporator (Whitman, Johnson, & Tomczyk, 2005). The evaporator will then directly affect condensing temperature in the PRL, whether heat is exchanged directly or if there is an intermediate process fluid.

3.3 Vapor Compression PID Tuning Drawbacks

The PID controller in a modern VCC uses software algorithms that take feedback information from a sensor or sensors and vary the algorithms' output in response (Whitman et al., 2005). For instance, the sensors may be a set of thermistors that monitor evaporator superheat. The output from the algorithm changes the output signal from the controller to the expansion valve, more or less refrigerant is allowed into the evaporator, and the cycle repeats. The proportional

controller monitors the evaporator superheat in relation to a desired set point and adjusts the electronic expansion valve in an attempt to decrease the error between the two. The integral algorithm calculates an average of the superheat over a period of time and makes adjustments to the electronic expansion valve to bring the average closer to the set point. The derivative algorithm calculates the rate of change in the superheat in the evaporator and the algorithm's output can help to respond quickly to rapidly changing load conditions. For a known and fixed load, PID tuning works especially well, as the best settings can be experimentally determined and then left fixed. For transient loads, response time becomes a bigger issue and condensing temperatures may change rapidly enough to adversely affect the pumped loop system pressure and thus other conditions such as mass flow rate.

There are at least two cost drawbacks to this type of control, especially when the response time needs to be as fast as possible. Equipment that can maintain conditions in a pumped loop condenser extremely close to a desired set point under varying loads is very expensive up front. Additionally, the maintenance cost and reliability problems for valves that are stressed from rapid and frequent opening and closing would likely be comparatively high to a setup that did not have valves at all. For these reasons, instead of coupling a VCC directly to a PRL that is cooling electronics, it makes more sense to use the VCC to make ice and couple an ice water heat sink to the PRL. Energy efficiency must also be considered, and will be addressed.

3.4 Experimental Setup

Figure 3.1 shows all of the components of the PRL, with the dashed enclosure being the area of interest and change between heat rejection options. The condenser in the figure was a brazed plate heat exchanger with 0.7 L volume on the pumped-loop side. The low-flow rotameter had an accuracy of ± 4 % of full scale flow. Four 300-W cartridge heaters were used to apply a load to the evaporator. The VCC was a commercial chiller (FTS Maxicool Model RC 100) that used R507 as its working fluid and was capable of maintaining a set point temperature at ± 0.1 °C under very stable conditions. The PRL evaporator consisted of 31 microchannels electro-eroded in the top of a copper block. Each channel had a length, width, and height of 13.3 mm, 0.139 mm, and 0.796 mm respectively. The cartridge heaters were coated with thermal grease for improved thermal contact and inserted into the bottom of the copper block.

Evaporator inlet pressure (P_{ei}), evaporator microchannel wall outlet temperature (T_{wo}), and condensing temperature (T_c) sensor locations are indicated in Fig. 3.1. The sensor monitoring P_{ei} was located in the inlet plenum of the evaporator just upstream of the microchannels and had a response time of 1 ms and accuracy of ± 3.4 kPa. The thermocouple monitoring T_{wo} was inserted in the copper block two millimeters directly below the outlet of the microchannels. The thermocouple monitoring T_c was externally mounted to the condenser with tape. Both thermocouples had accuracies of ± 0.5 °C. All of the tubing for the loop was 0.48-cm inner diameter (nominally quarter inch outer diameter in English Units), with the exception of the section between the outlet of the evaporator and the heat

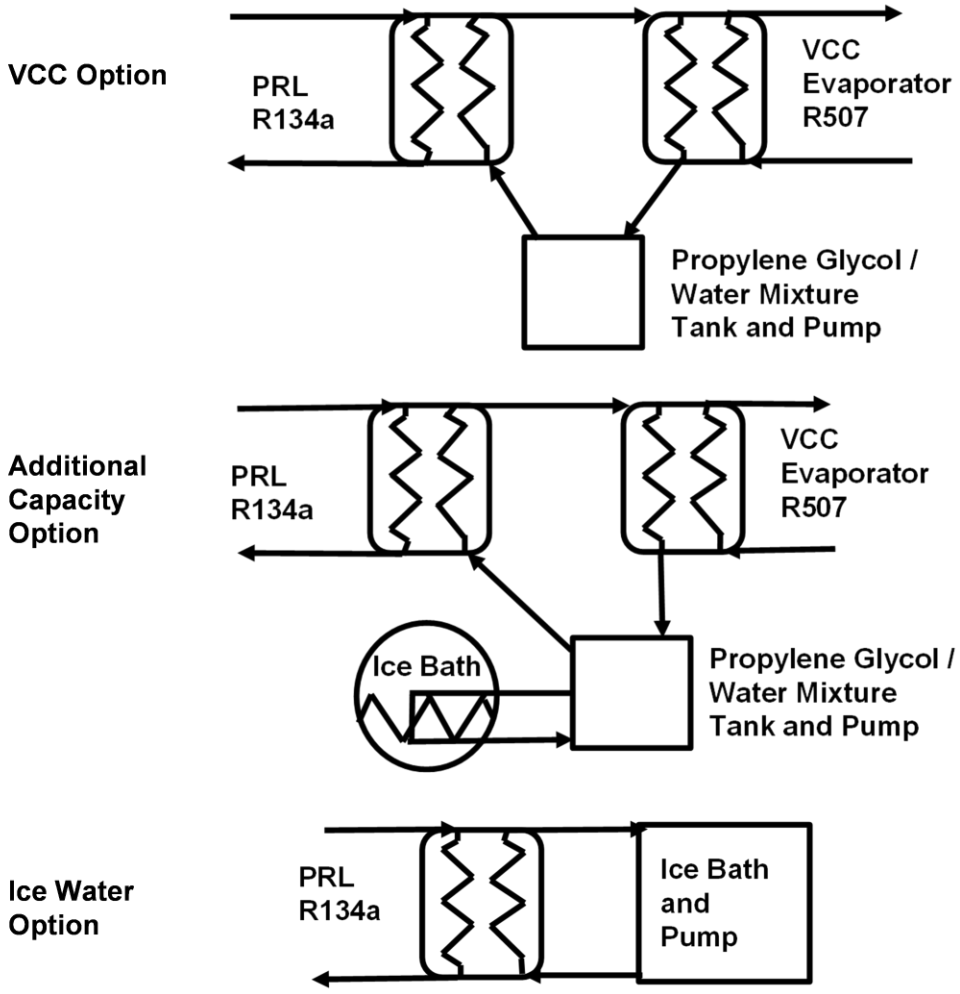

Figure 3.2. The heat sink options evaluated.

exchanger. This section was 0.76-cm inner diameter (nominally 3/8 inch outer diameter in English Units), which was done to allow more room for vapor expansion.

Figure 3.2 shows the heat sink setup options studied. The VCC option has the VCC as the heat sink with a propylene glycol and water mixture as the intermediate process fluid between the VCC and the PRL's condenser. This

option is very similar to using the condenser of the PRL as the VCC's evaporator. Any change in the VCC's evaporating temperature is transmitted to the PRL condenser rapidly via heat exchange with the propylene glycol and water mixture. The second setup, named the additional capacity option, shows the addition of an ice bath used to increase the capacity of the VCC. The third setup, named the ice water option, has the PRL exchanging heat with pumped ice water.

3.5 Method

The comparison between the additional capacity option and the VCC option is made using data from sequential experiments with identical conditions. For each of the experimental runs, the pumped loop was allowed to come to

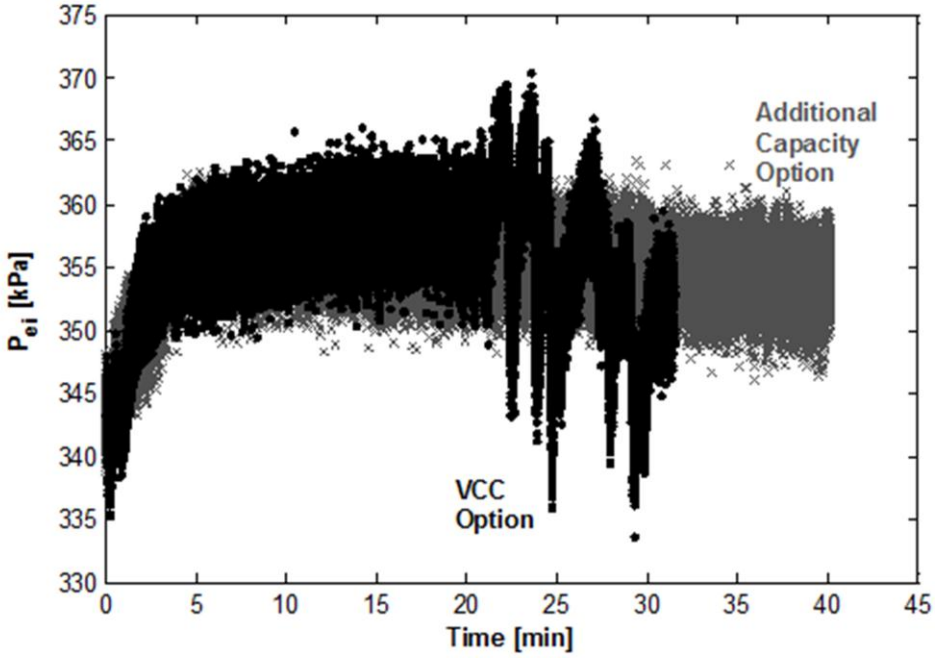

Figure 3.3. Evaporator inlet pressure comparison between the VCC option and the additional capacity option under identical loading and operating conditions.

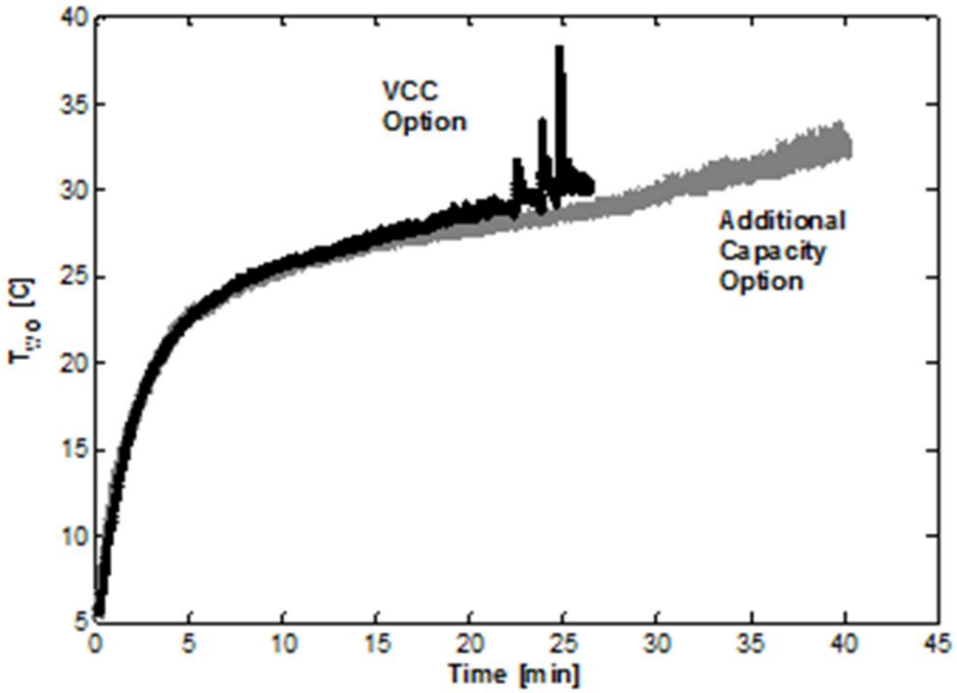

Figure 3.4. Evaporator microchannel outlet wall temperature comparison between the VCC option and the additional capacity option under identical loading and operating conditions.

steady state under no load. A step input of 198W was applied, and then no other changes were made until flow rate problems caused dry-out conditions and the heat input had to be shut off. The results from this comparison led to the complete elimination of the VCC and replacement with an ice bath; thus, the comparison between the VCC option and the ice water option is made using data from two separate attempts to reach CHF with similar operating conditions. For these two attempts, the evaporator started at steady, no load conditions, and step inputs in load were applied incrementally.

3.6 Results

3.6.1 Option Comparison

Figures 3.3 and 3.4 show results from both the VCC and the additional capacity option together as described above. With both options exposed to an initial step input of 198 W, the delay in time of instability development is substantial with the additional capacity option. With the VCC option, Fig. 3.3 shows pressure instabilities initiated by the PID controller causing early dry out to occur in the evaporator as shown by T_{wo} in Fig. 3.4. The additional capacity option delays the action of the PID controller algorithm, and stable conditions extend more than ten minutes beyond where the VCC option failed.

Figure 3.5 shows P_{ei} and heat flux (q'') changes when using the VCC option with incremental increases in heat flux. Figure 3.6 shows the corresponding T_c. Upon inspection of both figures, it is clear that the VCC strives to maintain a constant average condensing temperature no matter the load condition. Taken together, the two plots are a good representation of how conditions in the condenser affect the entire system. The local maxima and minima are coincidental in time between the two plots as a result of changes in the condenser affecting the system pressure. Conditions monitored within the condenser are saturated, so T_c will change exactly in accordance with the condensing pressure. This pressure change is transmitted throughout the system. This is a different phenomenon than the pressure rise induced by the pump, as the pump creates localized pressure changes between it and the evaporator. The magnitude of the changes in T_c are

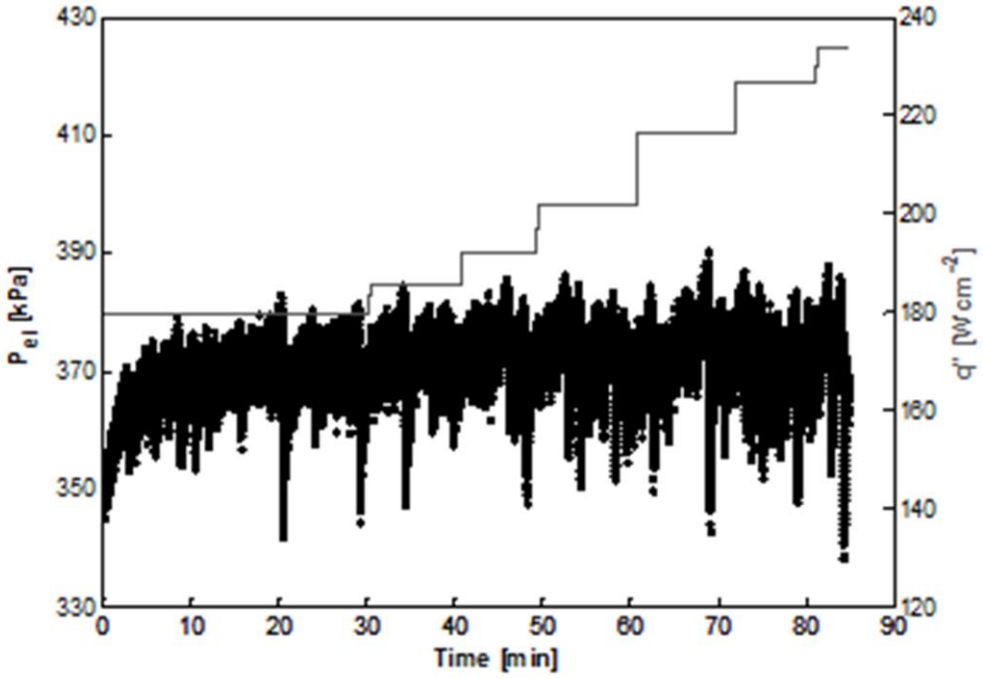

Figure 3.5. Evaporator inlet pressure during incremental increase of heat flux using the VCC option.

actually better represented by the magnitude of the changes in P_{ei} because of the pressure sensor's fast response time and direct exposure to refrigerant. As stated in the introduction, adjustments to pumping power had to be made continuously to offset the rapid, large pressure oscillations shown in Fig. 3.5. During this experimental run, the mass flux maintained through the evaporator was 300 kg m^{-2} s^{-1}, while for the ice water option discussed next, the mass flux was only 200 kg m^{-2} s^{-1}.

In contrast to the VCC option, the ice water option has a fixed capacity that depends on the ice water pump speed. This option may have an increasing PRL

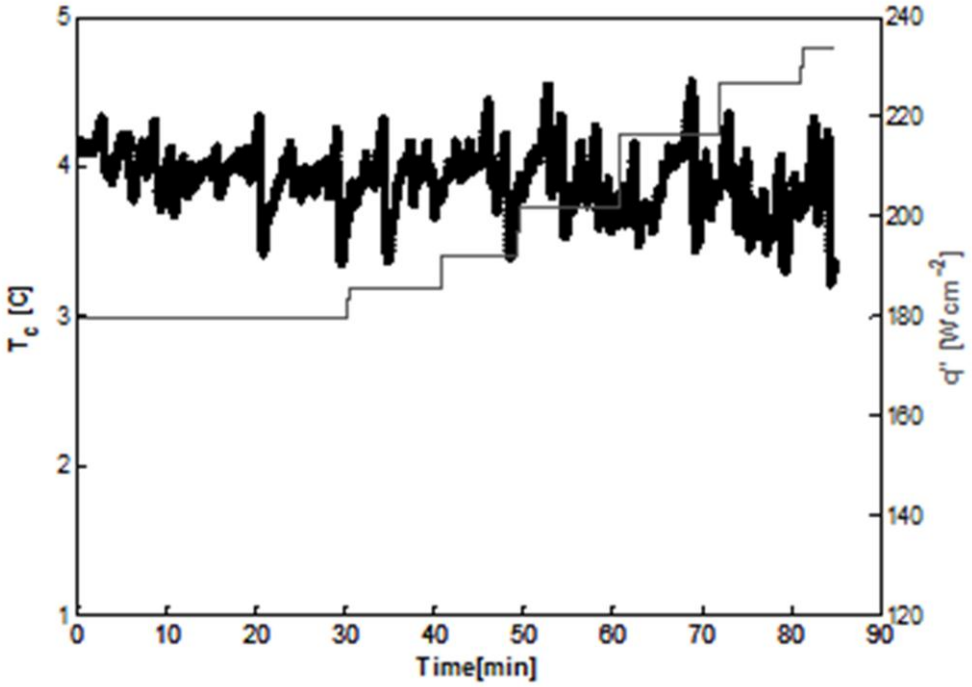

Figure 3.6. Condensing temperature during incremental increase of heat flux using the VCC option.

system pressure with additional loading, unless pumping power were increased with loading or the ice bath cycled between well and poorly mixed conditions. A gradual system pressure rise in response to higher heat flux in the evaporator is actually a convenient way to slightly suppress boiling, keeping qualities in lower ranges in the evaporator than if a constant system pressure is maintained. Increasing pumping power is to be avoided, as similar problems to those experienced with the PID tuning in the VCC option will occur. It is better to size the pump to provide a large enough fixed flow rate to minimize the condensing temperature increase for the expected load values, which is what occurred here. Figure 3.7 shows a steadily increasing evaporator inlet pressure, which is the natural progression as two-phase conditions develop in microchannels due to

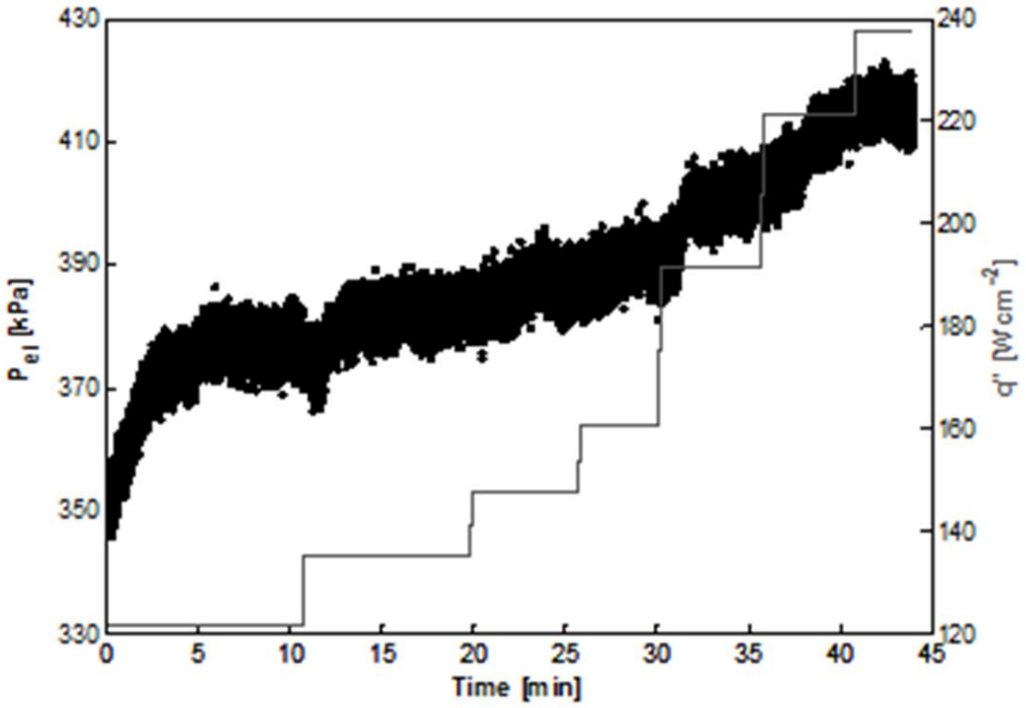

Figure 3.7. Evaporator inlet pressure during incremental increase of heat flux using the ice water option.

increasing friction and acceleration pressure losses. Figure 3.8 shows the gradual changes in T_c, which are explained by ice addition, ice mixing, and increased vapor production within the pumped loop during the experiment. The difference between the maximum and minimum values for T_c for the ice water case was only half of a degree Celsius (registered by an externally placed thermocouple on the condenser surface), and there were no severe or abrupt changes. In fact, the worst rate of change for the T_c values in the ice water case was only 0.3 °C over a period of 15 minutes. Revisiting Fig. 3.6, the VCC option has numerous severe changes to the slope of T_c that are greater than half a degree Celsius in magnitude in a time span of seconds. The pressure swings with the

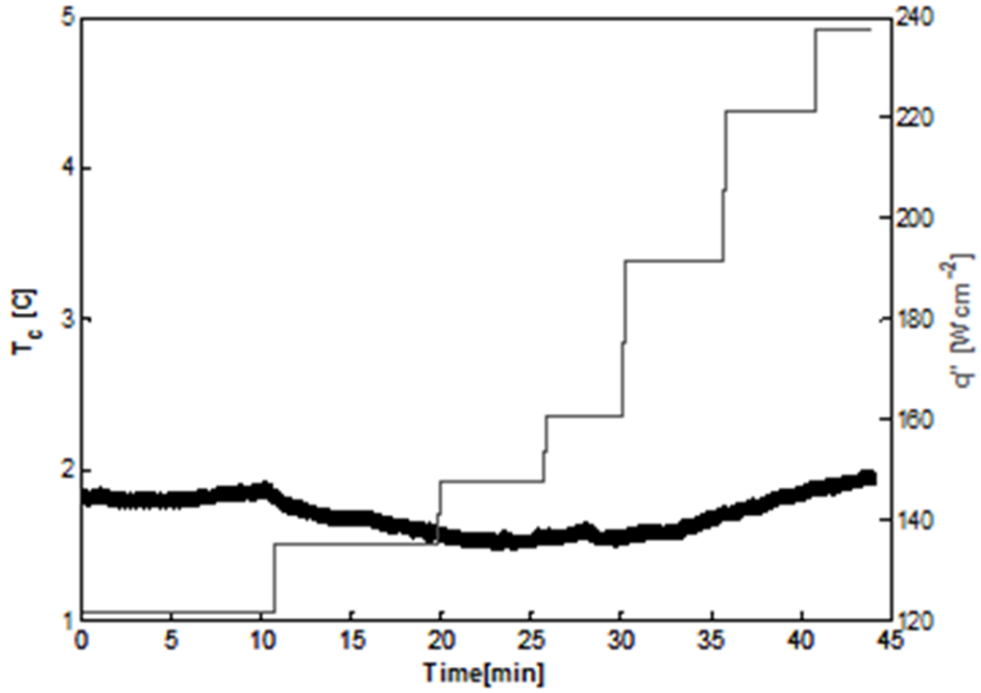

Figure 3.8. Condensing temperature during incremental increase of heat flux using the ice water option.

VCC option shown in Fig. 3.5 were up to 40 kPa, while for the ice water option, pressure changes were a quarter of that value.

Another benefit favoring the ice water option was the short time it took to achieve stable operating conditions within the pumped loop during system startup. Just as the PID controller in a VCC will adjust to meet loads during operation, it must do the same when first cooling the PRL from an off condition at room temperature. This process creates system-wide pressure fluctuations, and the result is a lengthy period of time to get liquid flow throughout the PRL. It was found that startup times could be reduced from 15 minutes or more with the VCC option to less than a minute with the ice water option. The best procedure was to

first start the ice water pump, allow it to cool the liquid maintained in the PRL condenser for a brief period of time, and then start the PRL refrigerant pump at a higher pumping power than eventually necessary to provide a high initial mass flow rate. This forced cold liquid refrigerant downstream as far as possible, avoiding the poor heat transfer coefficients of superheated refrigerant. Once the PRL loop was cooled, the refrigerant pump power could be reduced to the desired mass flow rate.

Assuming the ice water option maintains cold enough temperatures in the PRL evaporator for it to be a viable option for an intended application, the thermal storage energy saving potential should also be considered.

3.6.2 The Potential Cost Savings of Thermal Storage

A simple comparison of the potential energy use costs of the VCC versus the ice water option follows. As mentioned previously, with the VCC option, heat is rejected from a PRL directly to a VCC. The ice water option rejects heat from the PRL to an ice bath. The ice water option ultimately requires a VCC to produce the ice, thus a comparison can be made between one VCC having to work all the time (direct coupling) and one VCC that can take advantage of off-peak hours to over-produce ice (ice water option). Several assumptions are made. The final heat sink for both is the same unlimited water supply at 22 °C. Ice produced in the ice water option is perfectly insulated and does not gain heat from the environment. The VCC for both cases is modeled as an ideal VCC with a 32 °C condensing temperature and -10 °C evaporating temperature. The ideal VCC assumes saturated liquid at the exit of the condenser, isenthalpic expansion, saturated

vapor at the evaporator exit, and an isentropic compressor. The VCC's max capacity is 600 W.

A six-hour period is considered where the VCC must remove 300 W of heat for the first 3 hours and 600 W of heat for the second 3 hours. The first period is during off-peak hours in which the cost of electricity is 0.15 cents per kWh, while the second period is during peak hours in which the cost of electricity is 0.20 cents per kWh. To do this between the prescribed temperatures and using the ideal VCC model, the compressor work required is 87 W for 300 W of cooling and 175 W for 600 W of cooling. For the ice water option, it is decided to overproduce for the first 3 hours at 600 W and then use the excess 300 W capacity stored in ice during the second three hours to make up for only cooling at a 300 W capacity. For the VCC option, the VCC meets the demand in both 3 hour periods with no thermal storage possibility.

The total cost of operation for the 6 hours with the ice water option is $0.131 while the total cost with direct coupling is $0.144. It is a 10% savings in favor of the ice water option. For longer periods of time, larger systems, or variations on operating conditions, this would amount to a substantial amount of money.

3.7 Conclusions

The pumped refrigerant loop could be very stable for cooling electronics if it rejects heat to a constant temperature heat sink such as ice water. Small changes in system pressure affect mass flow rate and temperatures throughout the pumped loop. The small, rapid changes in system pressure in a PRL that accompany a PID controlling process if a VCC is directly coupled can lead to premature dry out as

two-phase flow progresses in the PRL evaporator. The ice water heat sink avoids these rapid changes, and is the most stable setup. Given the right operating conditions, the PRL with ice water cooling can be superior to the PRL with direct heat rejection to a VCC in terms of energy usage costs. Gradual condensing temperature rise and system pressure rise will be seen with the pumped ice water loop, but there is no associated instability. The PRL with direct heat rejection to a VCC will be able to maintain the same average set point, but aberrations caused by the PID controller can cause mass flow rate and dry out problems in the PRL. In summary, system startup time, energy usage cost, maintenance costs, and stability of system pressures and mass flow rate can all be improved in a pumped refrigerant loop when its vapor compression cycle is completely decoupled.

Chapter 4: Critical Heat Flux in Microchannels with an Adjustable Inlet Orifice

Abstract

The benefits of eliminating instabilities in two-phase microchannel flow with inlet orifices come with costs. This study describes the tradeoffs between microchannels with and without inlet orifices, focusing on results from critical heat flux data obtained for various orifice sizes and mass fluxes. An adjustable inlet orifice controlled with a micrometer was placed in front of an array of 31 parallel microchannels each with a hydraulic diameter of 0.235 mm and a length of 1.33 cm. For mass fluxes ranging from 186 kg m^{-2} s^{-1} to 847 kg m^{-2} s^{-1}, critical heat flux (CHF) data were obtained for 7 different orifice sizes. For low flow rates that provided a low quality saturated inlet condition, the difference in CHF values was found to be minimal between open and almost closed orifice conditions. The smallest orifice achieved a CHF value of 5 W cm^{-2} less than the largest orifice size for a mass flux of 186 kg m^{-2} s^{-1}, and 7 W cm^{-2} less for a mass flux of 433 kg m^{-2} s^{-1}. For mass fluxes higher than 433 kg m^{-2} s^{-1}, subcooled conditions were present at the orifice inlet, and the highest CHF values occurred with an orifice hydraulic diameter of 35 percent of fully open. For the higher mass flux cases, orifice sizes in the range of 1.8 percent to 28 percent of fully open caused CHF to occur at lower values than less restrictive orifice sizes. This was due to loss of cooling capacity from rapid pressure drop through the orifice. Slightly higher average channel pressures also decrease the refrigerant's latent heat of vaporization. For the orifice sizes from 35 to 70 percent of unrestricted flow, a very minimal increase in pressure drop over fully open inlet conditions occurred

and the general trend was higher CHF values. Very small inlet orifices are beneficial for steady state conditions that do not approach CHF; however, overly restricting the flow at the inlet to microchannels reduces cooling capacity significantly and will cause early onset of CHF. A slightly restrictive inlet orifice will increase CHF.

4.1 Introduction

Microchannel heat sinks with refrigerant as the coolant are an effective way to provide low temperature cooling for electronics. One problem that has been observed with microchannel two-phase cooling is a tendency for backflow to occur, reducing cooling effectiveness. Two causes of backflow are instabilities known as parallel channel and compressible volume (Bergles & Kandlikar, 2005). Inlet orifices in front of microchannels can reduce or eliminate instabilities (Park et al., 2009; Odom et al., 2011). To do so, they must create enough of a high pressure region at the entrance to the channels to block upstream movement of vapor or the redistribution of vapor among parallel channels known as parallel channel instability (Bergles & Kandlikar). A previous study conducted by the authors considered steady-state two-phase conditions not approaching CHF for 31 parallel microchannels electro-eroded in a copper block. Inlet orifices with a restricted-to-unrestricted orifice hydraulic diameter ratio (D_h:$D_{h,ur}$) of 35% and less showed lower wall temperature and slightly elevated average refrigerant temperatures. The result was a higher average heat transfer coefficient. The wall temperature sensors and the inlet pressure sensor showed reduced oscillations as well.

The benefits observed at lower heat flux come with costs as CHF is approached. The large pressure drop in front of the channels could cause a flashing effect to occur, especially if the inlet condition is subcooled only slightly (Park et al., 2009). Flashing is when refrigerant suddenly becomes a mixture of vapor and droplets. Flashing eliminates a portion of the refrigerant's latent heat of vaporization and draws heat from the surrounding liquid to affect the accompanying temperature drop. Eliminating a portion of the refrigerant's latent heat of vaporization is undesirable if CHF is approaching, as saturated conditions tend to have very high heat transfer coefficients during low quality conditions (Mahmoud, Karayiannis, & Kenning, 2011). As refrigerant moves into high quality or superheated states, the heat transfer coefficient reduces and microchannel wall temperatures rise. If the heat transfer coefficient reduces enough, CHF will ensue.

4.1.1 Literature Review

One study on the effectiveness of inlet orifice restrictions at reducing backflow during two-phase boiling conditions in microchannels by Kuan and Kandlikar (2006) used water as the cooling fluid and a small orifice at the start of each channel that provided a D_h:$D_{h,ur}$ ratio of 38%. They found one to two degrees of surface temperature improvement and reduction of backflow for mass fluxes that provided a large enough pressure drop to prevent movement of vapor into the inlet plenum area of their test section. Koşar, Kuo, and Peles (2006) put inlet restrictions of varying length (as opposed to varying orifice D_h), all with a D_h of 37 μm, into channels with a D_h of 227 μm. Their orifice ratio, D_h:$D_{h,ur}$ was

Table 4.1.

Inlet Orifice Effectiveness Studies.

Study	Micro-channel Material	Micro-channel D_h [mm]	D_h:$D_{h,ur}$ [%]	Working Fluid	Finding
Kuan and Kandlikar (2006)	Copper	0.33	38	Water	For steady-state conditions, backflow reduction and one to two degree surface temperature improvement for G = 362.9 kg m^{-2} s^{-1}. No improvement for G = 144.4 kg m^{-2} s^{-1}.
Koşar, Kuo, and Peles (2006)	Silicon	0.227	16	Water	Inlet restriction length varied. Unstable boiling delayed with increased length. Found an optimum length beyond which no further improvement seen.
Michel, Thome, and Park (2009)	Copper	0.315	63	R134a	For G = 1880 kg m^{-2} s^{-1}, increase in CHF of 10 W cm^{-2}. No improvement for G = 390 kg m^{-2} s^{-1}.

16%. They found that inlet restrictions tend to increase the heat flux necessary for pressure oscillations to occur. Park et al. (2009) reported on CHF values for R134a flow through microchannels formed by wire electron discharge machining in copper with a $D_{h,ur}$ of 315 µm. The inlet restrictor used had a D_h of 199 µm (providing a D_h:$D_{h,ur}$ ratio of 63%). For a mass flux of 390 kg m^{-2} sec^{-1}, they found no improvement in CHF with an orifice in place; however, for a mass flux of 1880 kg m^{-2} sec^{-1}, they achieved CHF values of approximately 10 W cm^{-2}

greater with the orifice in place (Park et al.). See Table 4.1 for a summary of these studies.

4.1.2 Objective

The primary objective of this paper is to provide further insight into what the optimum D_h:$D_{h,ur}$ should be for a parallel array of microchannels in order to maximize values of CHF.

4.2 Experimental Setup

4.2.1 Pumped Refrigerant Loop Configuration

Figure 4.1 shows the flow loop configuration used to obtain CHF data and evaluate heat transfer coefficients. After picking up heat in the test section, the R134a in the primary loop rejected heat to water pumped from an ice water reservoir. This method of heat rejection was found to provide very stable system pressures, and thus very stable mass flow rates. The site glass located just upstream of the test section was valuable for aiding in identifying whether the inlet conditions were subcooled or low quality vapor in the middle of experimentation. The bypass loop shown in the figure allowed the pump to be set at a slightly higher power input during very low flow rate experiments. This helped to keep the pump away from its minimum input power level. The bypass needle valve was another method of fine tuning the flow rate in addition to the rotameter outlet valve and adjusting pump speed. Power to the pump was controlled by a variable DC power source, in which the voltage applied could be minutely adjusted. This proved valuable during the approach to CHF, as pressure drop changes had subtle influences on mass flow rate.

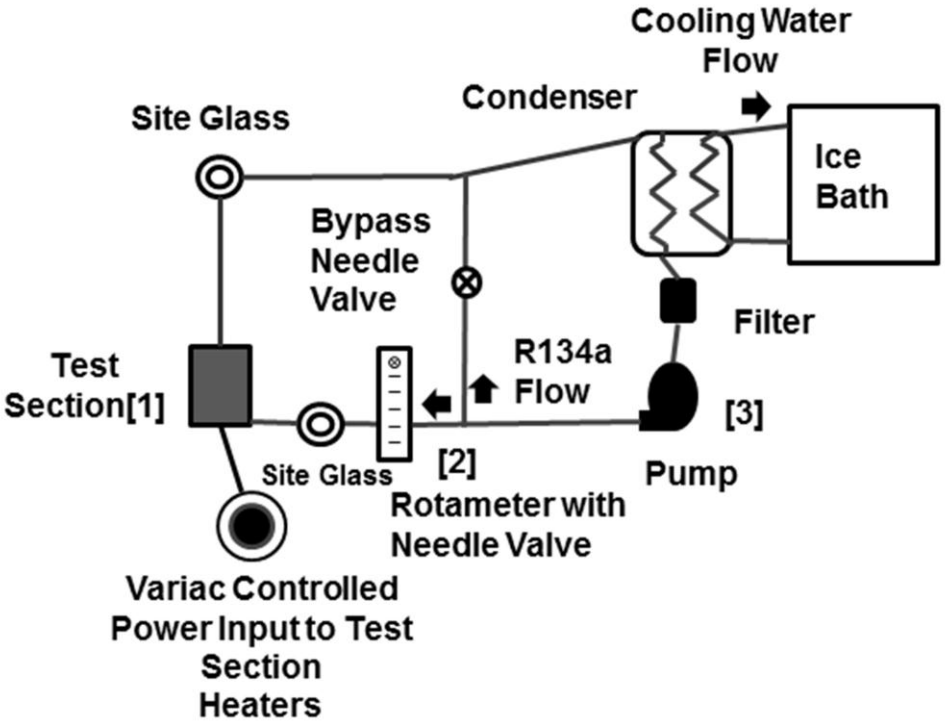

Figure 4.1. Pumped refrigerant loop configuration with numbers indicating sensor locations.

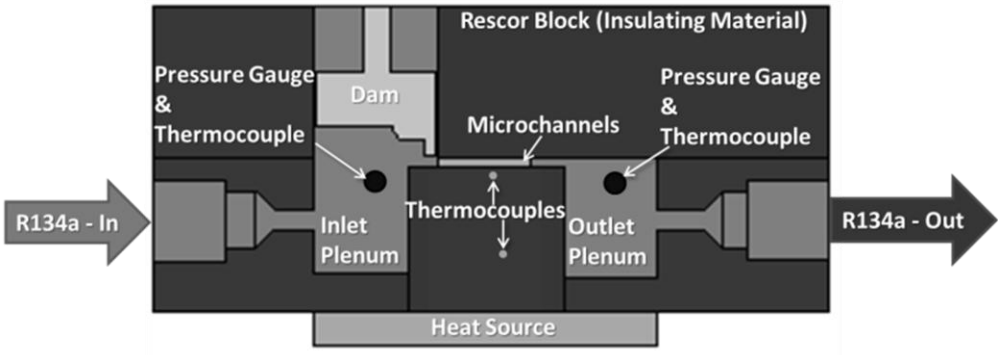

Figure 4.2. Side view of the test section. The adjustable orifice is created by a dam directly in front of a parallel array of 31 microchannels.

4.2.2 Test Section Design

A drawing of the test section is provided in Fig. 4.2. There are 31 parallel microchannels each of hydraulic diameter (D_h) 0.245 mm and length 1.33 cm, with a dam that can be raised and lowered immediately upstream of their inlets (the gap between the dam and the channels is approximately 100 microns). The dam combined with the walls of each individual channel provides an orifice for each channel, or the orifice can be thought of as the hydraulic diameter defined by the adjustable cross section beneath the foot of the dam. It is this latter definition that should be thought of when the term orifice is used for the remainder of the paper, and for plotting purposes the orifice size will be given as a percentage of fully open, unrestricted flow. The fully open D_h for the space beneath the dam is 1.4 mm, while the smallest size used to evaluate orifice effects (D_h:$D_{h,ur}$ = 1.8%) corresponds to a D_h of 0.0254 mm. A detailed description of the test section can be found in Odom et al. (2011). Several modifications were made since that description was written to be able to run CHF experiments. An O-ring groove was cut into the copper block just below the microchannels, creating a shaft type seal between the copper block and the Rescor 914 ceramic piece into which it fit. This brought the temperatures that the O-ring was exposed to down to a much more manageable level from the previous design. Additionally, two ungrounded K-type thermocouples in 1.6 mm (1/16 inch) diameter stainless steel sheaths were coated with thermal grease and placed in 1.6 mm holes drilled into the copper block outside of the pressure boundary. One thermocouple tip was located 1.02 cm (0.4 in) below the other with a constant cross-sectional area between them. This

enabled their use in Fourier's Law to find heat flux, in combination with the known conductivity of oxygen free copper. The thermocouple closest to the microchannels was 76.2 μm (0.003 in) below the very center of the microchannel array, giving a measurement of the microchannel average wall temperature.

4.2.3 Measurements and Uncertainty

Mass flow rate was measured by a rotameter with a repeatability of 1%. The rotameter was calibrated for R134a using a gravity driven method with two large recovery tanks. This method provided very steady flow rates and an accurate calibration of the instrument, with the total uncertainty estimated at 4% for any given mass flow reading. Heat flux was measured using Fourier's Law,

$$\frac{Q}{A} = \frac{k(T_l - T_w)}{L} \tag{1}$$

with a total uncertainty of plus or minus five percent of the measured value. The area used in this calculation and in all the figures was the base area for the microchannels (1.08 cm^2) as opposed to the total surface area for the channels. All thermocouples were calibrated and have an estimated uncertainty of ±0.5 °C. Pressure transducer accuracy is estimated at ±3.4 kPa.

4.3 Experimental Method

4.3.1 CHF Data Collection

Data were recorded for randomly ordered orifice sizes at each flow rate. Due to the ever increasing potential for damage to the test section as higher critical heat fluxes were attempted, all experimental runs at a flow rate were completed before continuing to the next flow rate value. Initially with a step heat input to the copper block, the two thermocouples used to find heat flux had different slopes

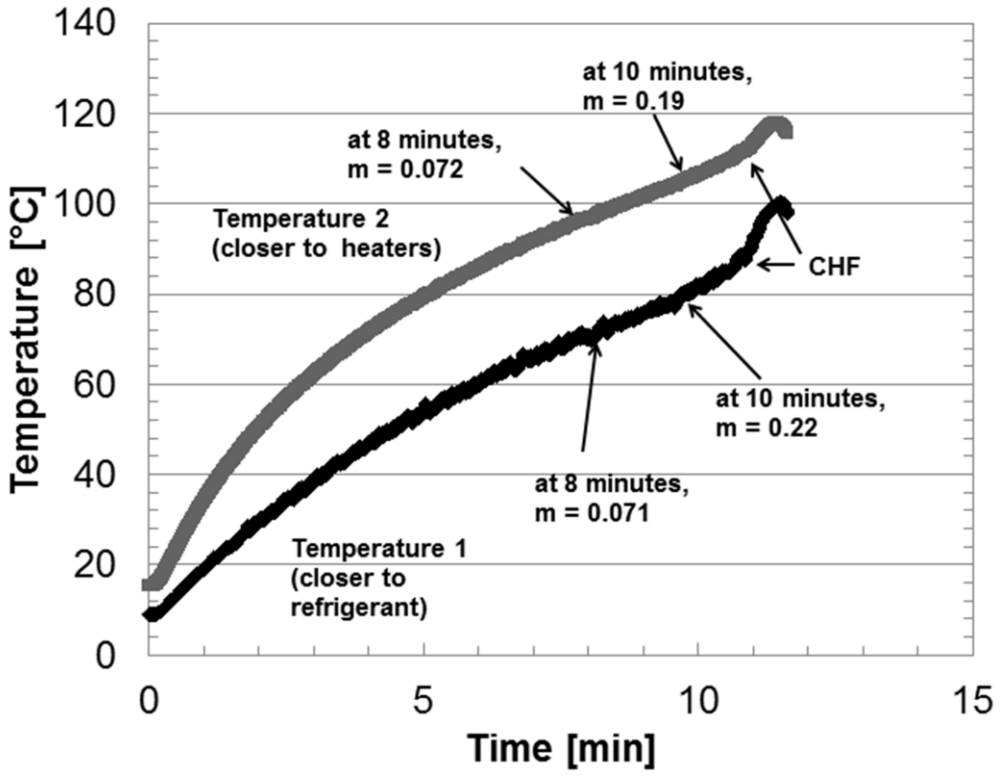

Figure 4.3. A representative plot depicting the quasi-steady state condition of the thermocouples used to calculate CHF using Fourier's Law.

for their temperature-time curves, but as CHF approached, the rate of change of temperature for the two thermocouples developed nearly identical values. A quasi-steady state was therefore assumed, and Fourier's Law was considered applicable. Figure 4.3 displays the typical progression for the two thermocouples through the occurrence of CHF. The slope, m, of each curve is shown at two locations. The high thermal conductivity of the copper combined with the relatively small thermal mass of the top portion between the two thermocouples allowed for a consistent linear distribution of temperature. The copper block as a whole provided a large thermal mass that could absorb large amounts of heat

without experiencing actual burnout such as an electronic device would when overheated. Identifying CHF became easy, as the heat flux calculated with Fourier's Law would pass slowly through a maximum point before beginning to drop simultaneously as a point of inflection in the average wall temperature occurred. For the lower flow rate experiments in which the outlet refrigerant temperature was superheated, refrigerant temperature would drop upon occurrence of CHF.

4.3.2 Characterizing the Orifice

If an orifice is inserted in the center of a pipe, upstream of the orifice the pressure drop will be essentially the same as the same pipe with no orifice installed. Pressure drop through the orifice will be relatively high, and so can the pressure drop downstream of the orifice due to downstream effects on flow conditions (Flow of Fluids, 1985). These facts allowed for calibration of the pressure drop caused by the orifice alone (downstream effects not included in the measurement) for the case of the refrigerant entering the orifice as subcooled liquid.

A flat top copper block was installed in place of the microchannel copper top (see Fig. 4.4). A 737 μm inner diameter pressure tap was placed just downstream of the orifice, liquid refrigerant was passed through at several mass flow rates and orifice sizes and data taken were used to develop a nomograph (Fig. 4.5) for estimating pressure drop caused by the orifice. This pressure drop estimation could then be used to get a better picture of the actual channel inlet pressure and temperature, instead of relying on the inlet plenum pressure and temperature

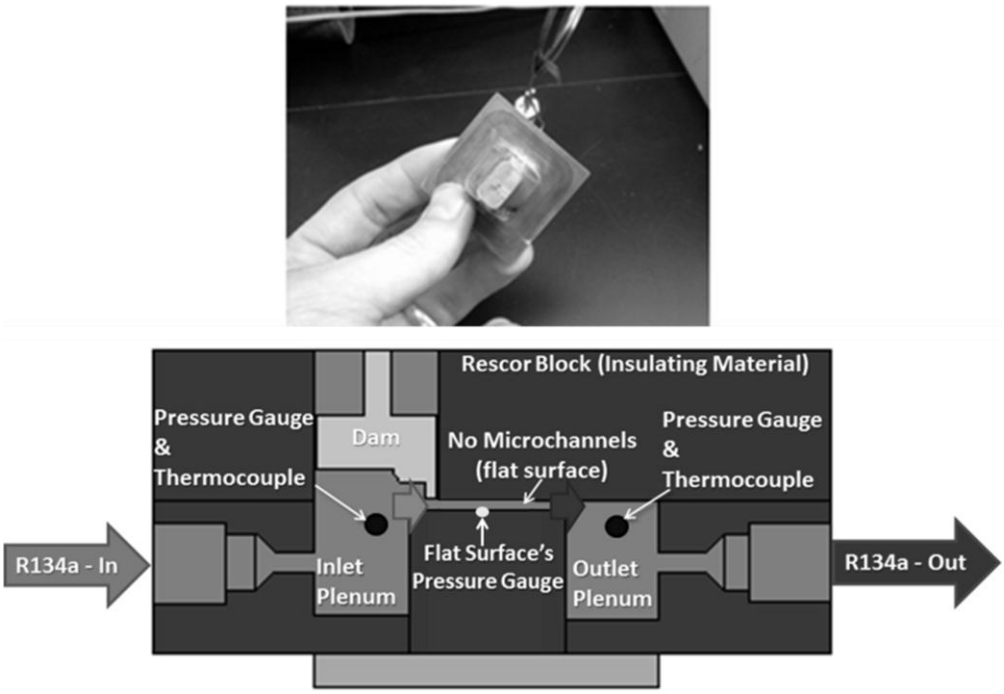

Figure 4.4. The flat surface with the pressure tap used for characterizing the orifice, and the associated modified test section diagram.

measurements for establishing the state of the refrigerant at the inlet of the channels (after passing through the orifice).

4.4 Results

Figure 4.6 shows the CHF values obtained for four different orifice D_h:$D_{h,ur}$ ratios. For lower mass fluxes, only the 1.8 % D_h:$D_{h,ur}$ and 100 % ratios were tested. For mass fluxes above 450 kg m^{-2} s^{-1}, conditions became subcooled in the inlet plenum of the test section and a trend in the data immediately emerged with the 35% D_h:$D_{h,ur}$ ratio having slightly higher CHF values than other ratios. The correlations plotted in Figure 4.6 are for reference and were chosen because they

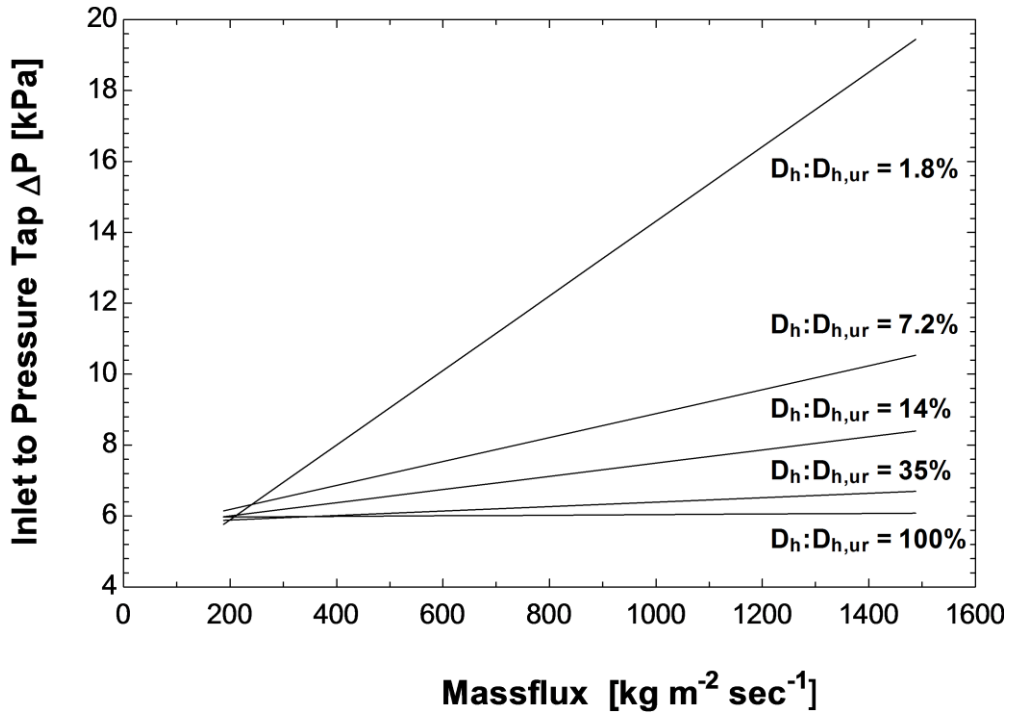

Figure 4.5. The nomograph developed to estimate pressure drop induced by the orifice at different sizes and mass fluxes.

both used R-134a as a cooling medium. The Basu and Ndao correlation was generated from data gained using stainless steel tubes with inner diameters of 0.5 mm, 0.96mm, and 1.60 mm over a wide range of conditions (Basu, Ndao, Michna, Peles, & Jensen, 2011). Wojtan and Thome (used single stainless steel microchannels of 0.5 mm and 0.8 mm inner diameter with both R-134a and R-245fa to develop their correlation (Wojtan, Revellin, & Thome, 2006).

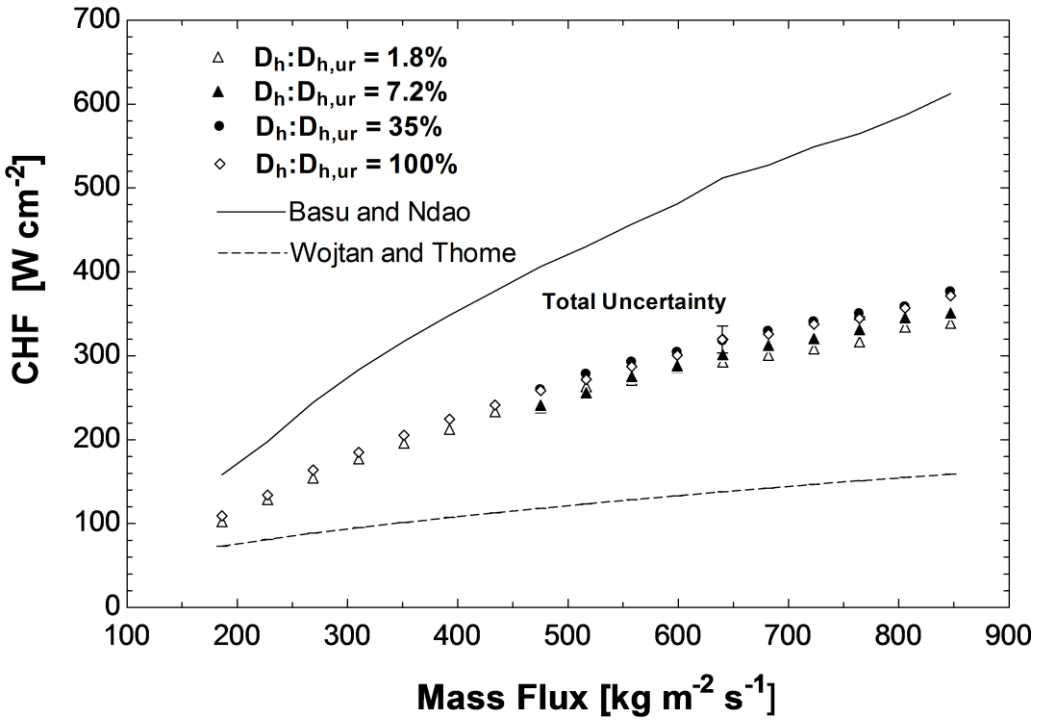

Figure 4.6. CHF for all mass fluxes tested. Beginning at 473 kg m^{-2} s^{-1}, 4 different orifice sizes are shown with D_h:$D_{h,ur}$ of 35% consistently achieving the highest CHF value.

4.4.1 Orifice Effect on CHF for Mass Fluxes of 186 kg m^{-2} s^{-1} to 433 kg m^{-2} s^{-1} with Saturated Inlet Conditions

Figure 4.7 shows the outlet refrigerant temperature ($T_{r,o}$) achieved for the 1.8% and 100% D_h:$D_{h,ur}$ ratios for mass fluxes between 186 kg m^{-2} s^{-1} and 433 kg m^{-2} s^{-1} with saturated inlet conditions. For the 1.8% D_h:$D_{h,ur}$ ratio, $T_{r,o}$ reached a lower value of superheat than for the 100% D_h:$D_{h,ur}$ ratio before CHF occurred. As a rule, the outlet pressure is lower for the orifice closed case, but pressure drop and average channel pressure is higher. The small orifice throttles the refrigerant,

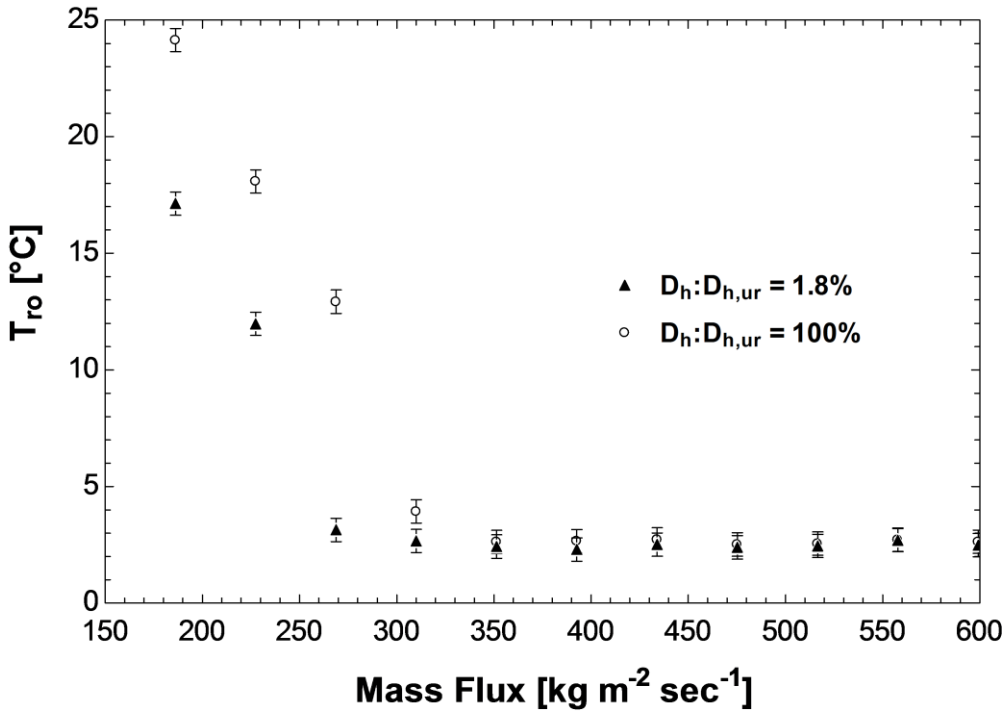

Figure 4.7. Outlet refrigerant temperatures at CHF for 1.8% and 100% D_h:$D_{h,ur}$ ratio, and outlet pressure of 3 bar.

speeding it up and increasing pressure drop. It is clear from the CHF data points that the almost closed orifice reduces capacity. Faster flow causes more refrigerant to be vaporized from pressure drop than in an unrestricted case, and thus dry out towards the outlet of the microchannels occurs at a lower heat flux. Instead of absorbing heat from the microchannel wall, the refrigerant that has converted to vapor in the orifice-almost-closed case has absorbed heat from the surrounding refrigerant, reducing wall temperatures early but exacting a toll on the overall ability of the refrigerant to cool. The refrigerant reaches a higher quality faster, reducing its ability to remove heat towards the outlet of the

microchannels. As stated in the introduction, for low heat flux conditions, flashing is a benefit, but as CHF is approached it becomes a drawback.

4.4.2 Orifice Effect on CHF for Mass Fluxes of 475 kg m^{-2} s^{-1} to 847 kg m^{-2} s^{-1} with Subcooled Inlet Conditions

Figure 4.8 shows the CHF achieved for the highest 6 mass fluxes tested with 3 intermediate D_h:$D_{h,ur}$ values in addition to those shown in Fig. 4.6. These additional orifice sizes were used to confirm that the 35% D_h:$D_{h,ur}$ ratio was emerging as the optimum size. The total uncertainty for the heat flux values shown in the figure is approximately ±5% of the measured value. This is almost solely due to bias error from uncertainty in exact thermocouple tip location. Using a single sample precision uncertainty estimate for q''(Beckwith et al., 1993)

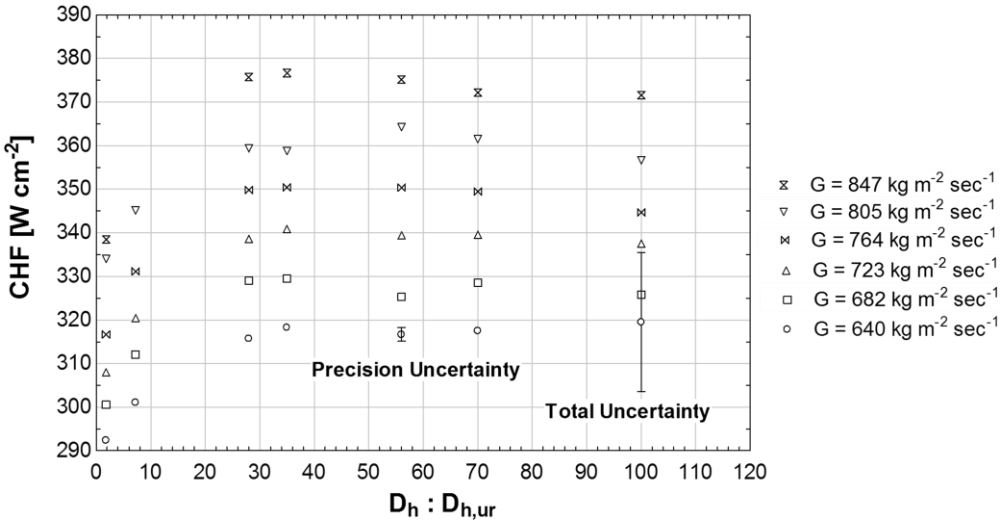

Figure 4.8. CHF for 7 different D_h:$D_{h,ur}$ ratios, at 6 different mass fluxes. Outlet pressure of 3 bar.

$$U_{q''} = 1.96\,\sigma_e \quad (95\%\ confidence) \tag{2}$$

and an estimate of standard deviation based on two replicates for many different orifice size and flow rate combinations, it is possible to plot a typical expected precision error for the data points in Fig. 4.8 as well. The precision uncertainty alone in terms of percentage of measured value is approximately $\pm$0.5% for the data points shown in Fig. 4.8 (+0.5% error at a measured value of 320 W is 1.6 W). The confidence in the trend shown through these data points is high, as the estimated precision error is less than half of the average difference in CHF, 3.6 W, between an orifice ratio of 35% D_h:$D_{h,ur}$ and the open orifice for the highest 10 mass fluxes shown in Figure 4.6.

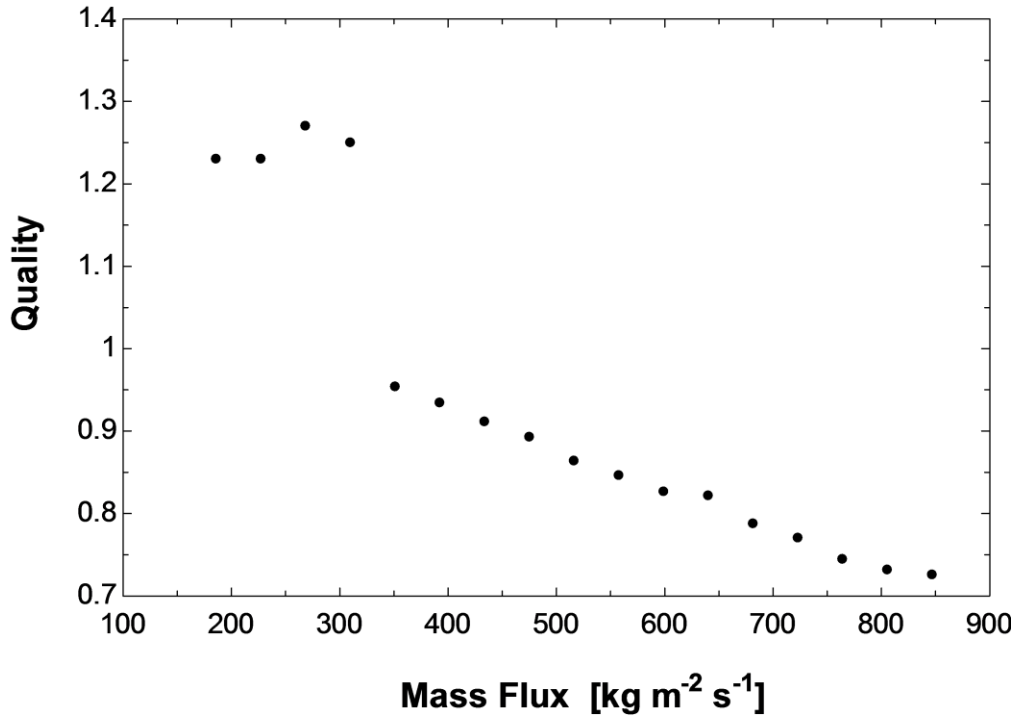

Figure 4.9. Outlet qualities for the 100% D_h:$D_{h,ur}$ ratio at CHF.

As a point of interest, Fig. 4.9 displays the outlet quality for the 100% orifice ratio at each mass flux tested. This figure indicates that CHF occurs at lower qualities for higher mass fluxes. This is due to the increased throttling effect that the microchannels have with higher mass fluxes, which will cause flashing just as an orifice does.

4.4.3 Heat Transfer Coefficient

The estimated total uncertainty for the average heat transfer coefficient, h_{avg}, in Fig. 4.10 is $\pm$5.5%, and the precision uncertainty is $\pm$2.2 %. The precision uncertainty alone is enough to disallow confident differentiation among very close values for the heat transfer coefficient. The largest contributor to the total uncertainty comes from the calculated heat flux value used to find the heat transfer coefficient. The average heat transfer coefficient shown in this plot is calculated as

$$h_{avg} = \frac{CHF}{\left(T_{w,avg}\text{-}T_{r,avg}\right)} \tag{3}$$

where $T_{w,avg}$ is the average wall temperature measured by the single thermocouple placed centrally beneath the microchannels. The average refrigerant temperature, $T_{r,avg}$, is based on the inlet and outlet plenum refrigerant temperatures, with the inlet plenum temperature adjusted in accordance with the nomograph shown in Fig. 4.5. In 6 of the 10 highest mass flux cases, the orifice at 35% D_h:$D_{h,ur}$ measured the highest heat transfer coefficient, twice h_{avg} was highest for the 1.8% D_h:$D_{h,ur}$, and twice for the 100% D_h:$D_{h,ur}$. This suggests that there is a trend for the 35% D_h:$D_{h,ur}$ to have the highest heat transfer coefficient as CHF is

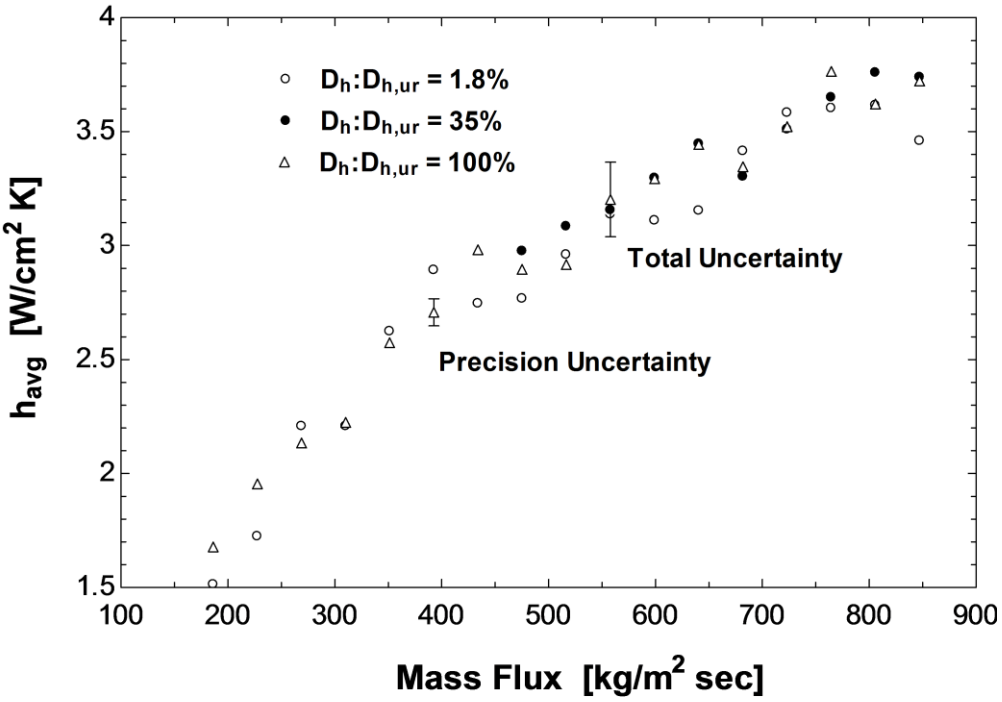

Figure 4.10. Average heat transfer coefficient, h_{avg}.

approached. Values for the heat transfer coefficient fall within the range of two phase heat transfer coefficients for R134a flow in microchannels published by Qu and Mudawar, where they found two-phase heat transfer coefficients to vary between 2 and 50 W cm^{-2} K, depending on quality and heat flux (Mudawar & Lee, 2005).

4.5 Analysis and Discussion

Reverting back to steady-state two-phase conditions in the microchannels in order to explain why the CHF trend is as seen above, the results of rapidly decreasing and increasing the orifice size from unrestricted to a 1.8% D_h:$D_{h,ur}$ under steady-state conditions for a mass flux of 1360 kg m^{-2} s^{-1} (mass flow rate, $\dot{m}$ of 4.58 ms^{-1}) are shown in Fig. 4.11. The orifice behaves similarly to an

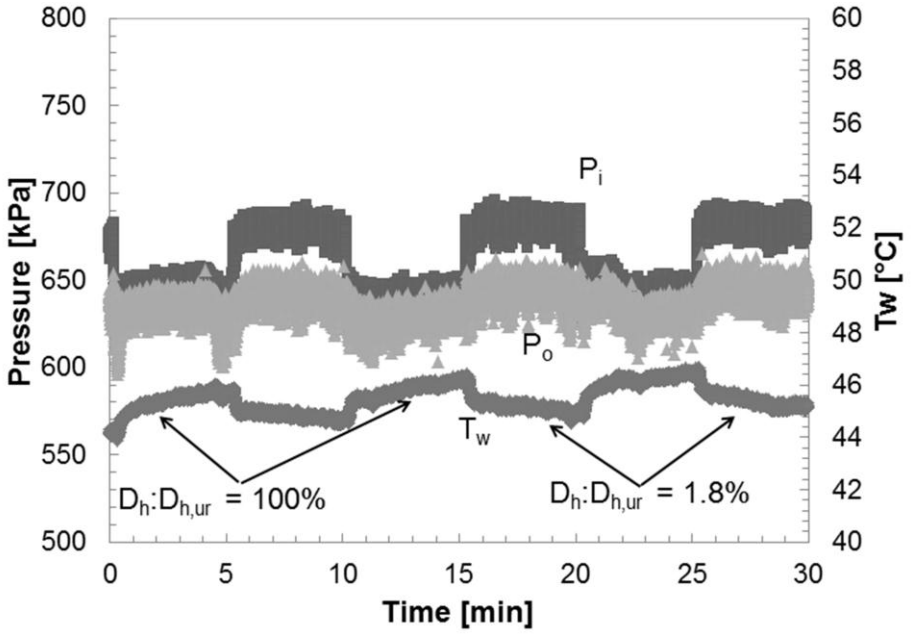

Figure 4.11. Rapid opening and closing of the orifice under steady-state conditions with mass flux of 1360 kg m^{-2} s^{-1} and heat flux of 225 W cm^{-2}.

expansion valve in a vapor compression cycle. For the 1.8% D_h:$D_{h,ur}$, there is higher pressure drop through the microchannels, higher average saturation pressure (and thus refrigerant temperature), but lower wall temperatures. It is not bulk refrigerant temperature that causes lower wall temperatures. It is a complex combination of flow velocity, flashing, higher pressures, and other variables that improve the average heat transfer coefficient during two-phase flow with inlet orifices in place.

To explain why flash gas appears in the microchannels, an energy balance that accounts for kinetic energy conversion to internal energy is performed using inlet

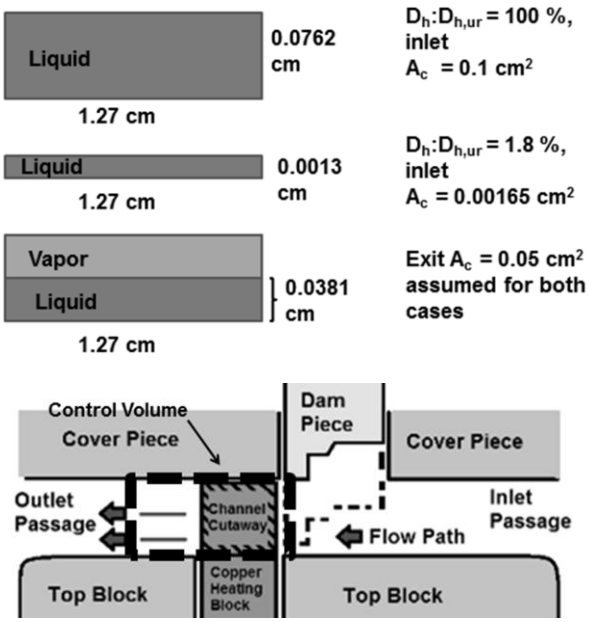

Figure 4.12. Inlet and outlet A_c used for refrigerant velocity estimation and the control volume used for the energy balance of Eqn. 5.

and exit conditions for the control volume depicted in Fig. 4.12 for each of the two orifice ratios of Fig. 4.11. Data from the 15 to 20 minute range are averaged for the 1.8% orifice ratio case, and data from the 20 to 25 minute range are averaged for the 100% orifice ratio case. The values of each measured parameter and calculated parameter of interest in the forthcoming example are shown in Table 4.2. The value for the inlet pressure in the 1.8% orifice case has been adjusted for an approximate 12 kPa orifice induced pressure loss. This pressure loss does not induce a change in temperature, as the isenthalpic throttling process for liquid R134a follows a line of constant temperature on a P-h diagram.

The velocity of the refrigerant immediately upon exiting the orifice is calculated for each orifice ratio using the cross sectional area, A_c, of the space beneath the dam depicted in Fig. 4.12 and the relation

$$v = \frac{\dot{m}}{\rho A_c} \tag{4}$$

where v is velocity, $\dot{m}$ is mass flow rate, and ρ is the density of liquid refrigerant. For the 1.8% case, the value of v just after leaving the orifice is halved to account for the possibility of a percentage of the flow passing around the dam rather than underneath. For the 100% orifice ratio, the A_c is 0.1 cm^2, and for the 1.8% orifice ratio, the A_c is 0.00165 cm^2. The A_c upon exit of the channels is estimated to be 0.0381 cm^2 for both cases, which is half of the exit passage A_c. The majority of the mass of the saturated mixture is assumed to still be liquid at this point, which is based on an energy balance for the 100% orifice ratio case.

After performing a steady state energy balance for the control volume, exit enthalpy is calculated as

Table 4.2.

Measured and calculated parameters of interest.

	D_h:$D_{h,ur}$ = 100%	D_h:$D_{h,ur}$ = 1.8%
P_i	639 kPa	665 kPa
P_e	629 kPa	640 kPa
T_i	6.3 °C	6.4 °C
v_i*	0.359 ms^{-1}	10.0 ms^{-1}
v_e*	0.718 ms^{-1}	0.718 ms^{-1}
Q_i	243 W	243 W
h_i*	60.5 kJ kg^{-1}	60.6 kJ kg^{-1}
h_e*	125 kJ kg^{-1}	175 kJ kg^{-1}
x_i*	0.0	0.0
x_e*	0.22	0.50

*calculated or retrieved from the property tables in Çengel & Boles (2008).

$$h_e = \frac{Q_i}{\dot{m}} + h_i + \frac{v_i^2 - v_e^2}{2} \quad (5)$$

Here, Q_i is the heat input to the microchannels, h_i and h_e are inlet and exit enthalpy, and v_i and v_e are inlet and exit velocity. With a known outlet pressure combined with the calculated enthalpies, exit qualities are estimated to be 0.23 and 0.50 for the 100 % and 1.8% orifice ratios, respectively. Therefore, in addition to velocity and average pressure differences between the two cases, the quality at which heat transfer occurs in the channels is different. As heat transfer coefficient is strongly dependent on quality (Lee & Mudawar, 2005), it is now clear why it is possible for an orifice to affect the heat transfer coefficient positively for lower heat fluxes, yet reduce CHF since high quality low heat transfer coefficient conditions appear earlier in microchannels with inlet orifices.

4.6 Conclusion

The effect of an inlet orifice on CHF was investigated for mass fluxes ranging from of 186 kg m^{-2} s^{-1} to 847 kg m^{-2} s^{-1} in 31 parallel microchannels of 235 μm D_h. An orifice is known to reduce or eliminate upstream compressible volume and parallel channel instability. For steady-state conditions at heat fluxes below CHF, dry out caused by reduction in capacity from the Joule Thompson process is not an issue. In those cases, smaller orifices provide higher heat transfer coefficients (approximately a 4% improvement) shown by reduced wall temperatures and slightly increased average refrigerant temperature through the channel.

The present study showed up to 5 W cm^{-2} of improvement in CHF for the highest mass flux tested, 847 kg m^{-2} s^{-1} when using a 35% of fully open flow-

sized orifice. This is only a 1% improvement in CHF. Out of 7 different orifice sizes at the highest 6 mass fluxes tested, critical heat flux reached the highest value for the D_h:$D_{h,ur}$ ratio of 35%. Fully open flow reached the highest value of CHF for only one of those flow rates, with the general result of any restrictive orifice between 35% and fully open being slightly better than a fully open orifice. The orifice size that showed the best wall temperature reduction under stable steady-state boiling conditions was too restrictive and caused an unnecessary reduction in cooling capacity for all flow rates considered. Summarizing, inlet orifices do not substantially improve heat transfer coefficients as CHF conditions develop in microchannels.

Chapter 5: Conclusions, Implications, and Further Research

5.1 Conclusions

An R134a pumped refrigerant loop (PRL) with an array of 31 microchannels and an adjustable inlet orifice was used to evaluate inlet orifice effectiveness at reducing oscillations, increasing critical heat flux (CHF), and improving heat transfer coefficients. The first part of the study, covered in Chapter 2, considered inlet orifice effect during steady-state-two-phase flow conditions. Chapter 3 addresses improvement of PRL stability in order to facilitate CHF experiments. Finally, in Chapter 4, inlet orifice effect on CHF was evaluated for a wide range of mass fluxes.

For steady-state-two-phase conditions, inlet orifices were shown to eliminate instabilities and increase heat transfer coefficients for D_h:$D_{h,ur}$ ratios of less than approximately 25%. The greatest improvement in heat transfer coefficient for steady-state experiments was for the smallest D_h:$D_{h,ur}$ ratio of 1.8 %. For a mass flux of 600 kg m^{-2} s^{-1} and heat flux of 337 W cm^{-2}, this ratio provided an increase in heat transfer coefficient of approximately 4%. For CHF experiments, the greatest improvement in heat transfer coefficient at the onset of CHF was approximately 1 % with a D_h:$D_{h,ur}$ ratio of 35%. For ratios less than this, CHF occurred at lower values with heat transfer coefficients decreasing by as much as 10%. The general conclusion from these two portions of the study is that optimally sized inlet orifices will show a mild positive effective on heat transfer coefficients and an ability to eliminate two-phase flow pressure oscillations.

During the course of improving the test section and PRL in order to be able to run CHF experiments, several PRL heat rejection setups were evaluated. By far, the ice water heat sink was superior to the other two setups that involved a vapor compression cycle (VCC) in terms of maintaining stable PRL system condensing temperature, system pressure, and mass flow rate. The PID tuning process inherent in the VCC was found to be the source of the problem, causing condensing temperature changes in the PRL. The result was system pressure drop and refrigerant vaporization in other locations in the loop. In addition to preventing rapid condensing temperature changes, the ice water heat sink was shown to have the potential for a 10% energy cost savings over a directly coupled VCC.

5.2 Implications

With only mild improvement in heat transfer coefficient attributable to inlet orifices, it would be easier to meet cooling demand by increasing mass flux; however, not all microchannel cooling devices will experience the same types or magnitudes of instabilities. For instance, Wang, Cheng, and Bergles (2008) found that the inlet configuration of a parallel microchannel cooling device can have a significant impact on oscillations. Therefore, the decision to include an inlet orifice in a microchannel cooling device should be predicated by research that shows the design is instability prone. Instabilities experienced in the microchannel array in the experiments described in this thesis (once an ice water heat sink was used) did not present a danger of equipment damage as there were neither pressure oscillations in excess of 15 kPa for all mass flow rates tested, nor were

Table 5.1.

A qualitative comparison between installing an orifice and increasing mass flow rate to improve the performance of a parallel array of microchannels.

Desired Effect	Do Orifices Achieve Desired Effect?	Cause	Does Mass Flow Rate Increase Achieve Desired Effect?	Cause
Oscillation Reduction	Yes	Orifice creates a pressure wall at inlet to channels as well as increased pressure drop through the channels, promoting downstream movement of vapor	Yes	Will decrease exit quality and thus onset of unstable boiling as well as increase pressure drop through the channels; however, not as effective as an orifice for preventing parallel channel instability
Wall Temperature Reduction	Yes (for Steady-State Conditions)	Improved heat transfer coefficient from higher inlet velocity and early transition to two phase conditions (increase in flash gas)	Yes	Improved heat transfer coefficient from higher inlet velocity
CHF Increase	No	Significantly increased flashing of refrigerant eliminates a portion of latent heat of vaporization and the associated high heat transfer coefficient as CHF is approached	Yes	Reduced enthalpy rise of refrigerant maintains lower quality conditions through higher heat fluxes than when using an orifice

there significant wall temperature oscillations. Table 5.1 is included to qualitatively summarize the differences between installing inlet orifices in front of each individual channel and simply increasing the mass flow rate to meet heat transfer requirements. An inlet orifice provides slightly reduced wall temperatures at steady-state conditions below CHF because refrigerant velocity is increased, average channel pressure is increased, and early transition to high heat transfer coefficient two-phase conditions occurs. The large kinetic energy of the high velocity refrigerant exiting the orifice is converted to internal energy during the

rapid head loss experienced as the refrigerant passes through the channels. Since conditions are two-phase as the conversion is happening, the result is sudden vaporization of the refrigerant. This is detrimental as CHF is approached, as the refrigerant passes into high quality conditions earlier than if mass flow rate was increased. There are numerous good studies of parametric effects on heat transfer in microchannels that support the qualitative description of increased mass flow rate (and thus velocity) effects. For instance, Lee and Mudawar (2008) found that the increased momentum from increasing mass flow rate of HFE 7100 in microchannels tended to overcome the large pressure drop created from vapor production that promoted upstream movement into their inlet plenum. Kuo and Peles (2009) investigated pressure effects on instabilities in microchannels, and found that increasing the average pressure in microchannels damped the magnitudes of pressure oscillations and mildly improved the stability of substrate surface temperatures close to the microchannel inlets. Both inlet orifices and increasing mass flow rate will have similar advantages in this regard as both increase the average channel pressure; however, inlet orifices will maintain a larger pressure drop immediately in front of the microchannel inlets, possibly making them superior to increasing mass flow rate for suppressing parallel channel instability.

To avoid CHF conditions, mass flux can be increased beyond the highest mass flux tested here of 847 kg m^{-2} s^{-1} with pressure drop across the test section (without an orifice installed) still expected to be manageable. As a point of reference, pressure drop across the test section for the 847 kg m^{-2} s^{-}1 mass flux

was still less than 30 kPa upon occurrence of CHF for unrestricted flow. If an orifice is still desired to keep the lowest flow rate possible combined with highest heat transfer rate, results indicate an orifice size in close proximity to the D_h:$D_{h,ur}$ orifice of 1.8% is best. This suggestion assumes the load remains known and stable, without rapid elevations that might lead to CHF.

5.3 Further Research

The test section built for this study remains capable of future experimentation. Without modification, higher mass flux experiments can be run to confirm the hypotheses that improvements in heat transfer coefficient with the optimum orifice size in place will remain less than 4% over unrestricted flow as CHF is approached. The copper block has a linear thermal expansion coefficient twice that of the Rescor 914 ceramic material that it rests inside of, so there is potential for cracking the ceramic as heat flux increases. It may be better to use the test section for other experiments before trying to run higher heat flux. For an improved statistical picture of the difference in heat transfer coefficient between the optimum D_h:$D_{h,ur}$ ratio and open flow, a large sample size could be gathered at a single mass flux. Different refrigerants could be tested to determine how various parameters influence the orifice effectiveness.

This test section can also be used in a two-test section pumped refrigerant loop to further understanding of pumped loop stability. A second test section for use in expanding microchannel studies has been built recently, and the pumped loop should be redesigned to include a valve system that allows both test sections to be used individually or simultaneously. The new pumped loop should be

compact so as to minimize the volume of refrigerant between the pump and the test section, reducing the possibility of a compressible volume instability. A pump capable of producing lower flow rates would enhance the ability to run very low flow rate experiments, and eliminate the necessity of controlling flow with the rotameter outlet valve. This would eliminate flashing between the rotameter and the test section from pressure drop in the rotameter outlet valve, and may enable placement of the rotameter or digital flow meter upstream of pump.

To improve accuracy in the reported values of heat flux for this and next generation test sections, an analytical model of the top portion of the copper heating block should be developed. This could be used to validate that Fourier's Law is usable to calculate CHF under the transient conditions mentioned in Chapter 4.

REFERENCES

Basu, S., Ndao, S., Michna, G. J., Peles, Y., Jensen, M. (2011). Flow Boiling of R134a in Circular Microtubes—PartII: Study of Critical Heat Flux Condition. *Journal of Heat Transfer, 133*, 1-9.

Beckwith,T. G., Marangoni, R. D., Lienhard V, J. H. (1993). *Mechanical Measurements, Fifth Edition.* Reading: Addison-Wesley Publishing Company, Inc.

Bergles, A. E., Kandlikar, S. G. (2005). On the Nature of Critical Heat Flux in Microchannels. *Journal of Heat Transfer, 127,* 101-107.

Boure, J.A., Bergles, A. E., Tong, L. S. (1973). Review of Two-Phase Flow Instability. *Nuclear Engineering and Design, 25,* 165-192.

Çengel, Y. A., Boles, M. A. (2008). *Thermodynamics, An Engineering Approach, Sixth Edition.* Boston: McGraw Hill.

Incropera, F. P., DeWitt, D. P. (1996). *Introduction to Heat Transfer*. New York: Jon Wiley and Sons.

Kirschman, R. K. (1985). Cold electronics: an overview. *Cryogenics, 25,* 117.

Koşar, A., Kuo, C., Peles, Y. (2006). Suppression of Boiling Flow Oscillations in Parallel Microchannels by Inlet Restrictors. *Journal of Heat Transfer, 128,* 251-260.

Kuan, W. K., Kandlikar, S. G. (2006). Experimental Study on the Effect of Stabilization on Flow Boiling Heat Transfer in Microchannels. *Proc. 4th International Conference on Nanochannels, Microchannels and Minichannels, Paper No. ICNMM2006-96045* Limerick, Ireland: ASME.

Kuo, C. J., Peles, Y. (2009). Pressure effects on flow boiling instabilities in parallel microchannels. *International Journal of Heat and Mass Transfer, 52,* 271-280.

Lee, J., Mudawar, I. (2005). Two-phase flow in high-heat-flux micro-channel heat sink for refrigeration cooling applications: Part II—heat transfer characteristics. *International Journal of Heat and Mass Transfer, 48,* 941-955.

Lee, J., Mudawar, I. (2008). Fluid flow and heat transfer characteristics of low temperature two-phase micro-channel heat sinks—Part 1: Experimental methods and flow visualization results. *International Journal of Heat and Mass Transfer, 51,* 4315-4326.

Lee, J., Mudawar, I. (2009). Low-Temperature Two-Phase Microchannel Cooling for High-Heat-Flux Thermal Management of Defense Electronics. *IEEE Transactions on Components and Packaging Technologies, 32*, 453-465.

Liu, J., Kaihua, G. (2010). Transient performance investigation of the mechanically pumped cooling loop (MPCL) system. *International Journal of Refrigeration, 33,* 26-32.

Lynn, P. A. (1998). *Introductory Digital Signal Processing with Computer Applications.* New York: John Wiley & Sons.

Mahmoud, M. M., Karayiannis, T. G., Kenning, D. B. R. (2011). Surface Effects in Flow Boiling of R134a in Microtubes. *International Journal of Heat and Mass Transfer, 54*, 3334-3346.

Odom, B. A., Miner, M. J. Ortiz, C. A., Sherbeck, J. A., Prasher, R. S., Phelan, P. E. (2011). *Microchannel Two-Phase Flow Oscillation Control with an Adjustable Inlet Orifice.* Manuscript submitted for publication.

Park, J. E., Thome, J. R., Michel, B. (2009). Effect of Inlet Orifice on Saturated CHF and Flow Visualization in Multi-microchannel Heat Sinks. *Proc. 25th Annual IEEE Semiconductor Thermal Measurement and Management Symposium.* San Jose, California: IEEE.

Phelan, P.E., Gupta, Y., Tyagi, H., Prasher, R.S., Cattano, J., Michna, G. et al. (2010). Optimization of Refrigeration Systems for High-Heat-Flux Microelectronics. *ASME Journal of Thermal Science & Engineering Applications, 2,* 1-6.

Qu, W., & Mudawar, I. (2003). Measurement and prediction of pressure drop in two-phase micro-channel heat sinks. *International Journal of Heat and Mass Transfer, 46,* 2737-2753.

Ulrich, R. K., Brown, W. D. (2006). *Advanced Electronic Packaging.* Piscataway: John Wiley & Sons, Inc.

Wang, G., Cheng, P., Bergles, A. E. (2008) Effects of inlet/outlet configurations on flow boiling instability in parallel microchannels. *International Journal of Heat and Mass Transfer, 51,* 2267-2281.

Whitman, W. C., Johnson, W. M., Tomczyk, J. A. (2005). *Refrigeration and Air Conditioning Technology 5th Edition.* Clifton Park: Thompson Delmar Learning.

Wojtan, L., Revellin, R., Thome, J. (2006). Investigation of Critical Heat Flux in Single, Uniformly Heated Microchannels. *Experimental Thermal Fluid Science, 30,* 765–774.

Flow of Fluids Through Valves, Fittings, and Pipe (1985). Technical Paper No. 410. New York: Crane Co.

APPENDIX A

PERMISSION STATEMENT

Brent Odom is the lead author for all material incorporated into Chapters 2-4. All coauthors have granted permission for use of the material in this dissertation.